Bull. Chem. Soc. Jpn., 75, 2309–2336 (2002)

Accounts

Stereodynamics of O(^{1}D) and O(^{3}P) Reactions Studied via Doppler-Resolved Polarization Spectroscopy

Yo Fujimura,* Hiroshi Tsurumaki, and Okitsugu Kajimoto*

Department of Chemistry, Kyoto University, Sakyo-ku, Kyoto 606-8502

(Received July 4, 2001)

Studies on stereodynamics of the gas-phase elementary reactions of atomic oxygen, O(^{1}D) and O(^{3}P), with simple molecules are reviewed. The angular correlations among the relative velocity vectors of reactants (**k**) and products (**k′**), and the product rotational angular momentum vector (**j′**) have been investigated via Doppler-resolved polarization spectroscopy. In the O(^{1}D) reactions with hydrocarbons and water, OH products are scattered into wide angular range and rotate mainly in the **k**–**k′** scattering plane. These angular distributions suggest the formation of an H–O–X (X = C or O) bond in reactive intermediates. By contrast, the NO products of the O(^{1}D) reaction with N_2O have isotropic angular distribution of **j′**, which indicates the participation of the out-of-plane motion in addition to the in-plane motions within the complex. These trends of O(^{1}D) reactions are consistent with the feature of product-state distribution of the individual reactions. Similar analyses for the reactions of O(^{3}P) atom with hydrocarbons have revealed that these reactions are not always dominated by the simple rebound abstraction mechanism based on the triatomic picture, which has long been assumed. As a background of the titled study, this account reviews the progress in the studies on gas-phase chemical reaction dynamics and presents the theory and techniques to investigate the stereodynamics of bimolecular reactions.

Studies on gas-phase chemical reaction dynamics aim to develop an understanding of the essential factors governing reactivity and energy disposal in the elementary reactions.[1–4] For this purpose, quantum-state resolved chemical dynamics has been investigated to elucidate how the reactions proceed on potential energy surfaces (PESs). This approach originated from the Eyring's pioneering "transition state theory" in the 1930's, which stated that the rate of chemical reactions can be *a priori* evaluated from the knowledge of PESs.[5] In the transition state theory, the reaction rates are calculated by applying the statistical method. Apart from the statistical approach, detailed studies of chemical reaction dynamics have successfully revealed the underlying factors determining the rate and dynamics on the PES as briefly reviewed below. Elucidating how chemical reactions proceed on PESs is also important to understand the mechanism of the complex reactions relevant to atmospheric chemistry[6] and combustion chemistry.[7] Furthermore, recent development of the laser control of chemical reactions deeply relies on the knowledge accumulated in reaction dynamics studies.[8]

The first success to relate the product state distribution with the dynamics on the PES was achieved by Evans and Polanyi in 1939.[9] They inferred that the vibrationally excited NaCl molecules produced from Cl + Na_2 reactions were the sources of the electronically excited Na atoms which emitted the D-line in Na-diluted flame. The vibrational excitation of NaCl was explained by considering the type of energy release on PESs; early energy release on the "attractive" surface promoted the vibrational excitation while late energy release on the "repulsive" surface enhanced the translational excitation. After some decades, the developments of the crossed molecular beam technique[10,11] and of infrared (IR) detection of chemiluminescence[12] made it possible to experimentally observe the nascent reaction products in the angular- and state-resolved manners, respectively. The information derived from these two methods was different and thus they complemented each other in studying chemical reaction dynamics of various reaction systems. The state-resolved measurements thus undertaken revealed that quite a few reaction systems yielded characteristic scattering angle distributions and nonstatistical product-state distributions. The results showed that chemical reactions were not always statistical, as assumed in the evaluation of rate constants based on the transition state theory.[13] Several prototypes of nonstatistical reactions were found, in contrast to the long-lived complex mechanism, which is considered to generate the statistical product-state distributions. They were, for example, harpoon, direct abstractions (rebound-type and stripping-type), and direct insertion followed by prompt bond rupture. The classification based on such molecular-collision-level observations added useful concepts for understanding chemical reaction dynamics.[1,2,14–16] The Nobel Prize was awarded in 1986 to Herschbach, Lee, and Polanyi to acknowledge the accomplishment of such studies on chemical reaction dynamics.[17,18]

A new frontier beyond the limited product-state resolution in crossed molecular beam was opened by the advent of laser techniques,[19] although the universal mass spectrometric detections in crossed molecular beam experiments are still quite useful.[20–22] The laser method has been extensively utilized in the studies on chemical reaction dynamics since the 1970's.[23] The high frequency-resolution of lasers has largely enhanced the ability of the rovibrational state selection in the detection of the reaction products. In addition, the products in the vibrationally ground state, which is invisible in the IR method, can be detected by laser excitation. Product-state distributions of numerous unimolecular and bimolecular reactions have been investigated and the knowledge of individual reactions continues to be accumulated.[1,4,24–28] Furthermore, high-quality polarization of laser light is also powerful to create and probe the spatial anisotropy and rotational angular momentum polarization.[29–34] Thereby, lasers have been playing significant roles, especially in stereodynamics investigation,[35–39] which is the main concern of this account. In laser experiments, a good number of new detection methods have been developed and nowadays laser facilities are combined with various types of molecular beam machines. State-of-the-art experiments have been performed with such modern pieces of apparatus and the finest results thus obtained for simple triatomic systems are rigorously compared with the high-precision theoretical calculations. Schneider et al. have succeeded in very sharp tuning of the collision energies for the $H + D_2 \rightarrow HD + D$ reaction by utilizing two parallel molecular beams of HI and D_2.[40] The single speed H atoms generated by the photodissociation of HI collide with the neighboring D_2 molecular beam and product D atoms are detected with the Rydberg-tagging method,[41] yielding high-resolution time-of-flight (TOF) spectra which resolve the rovibrational states of the sibling HD products. The differential cross sections (DCSs) thus measured with a rotatable detector have shown almost perfect agreement with the theoretical calculations of the highest quality to date.[40,42–45] Recently, Yang and coworkers have applied the same technique to $O(^1D) + H_2$ reaction using O_2 and H_2 beams by utilizing photodissociation of O_2.[46,47] The state resolution of sibling OH products measured by Rydberg H-atom TOF is sufficient to show that the DCSs are strongly dependent on the OH rovibrational levels. Liu and coworkers have constructed a variable angle crossed molecular beam machine capable of fine tuning of collision energies.[48] This machine extracts DCS from the H-atom velocity mapping with its Doppler-resolved TOF detection method.[49] Furthermore, by monitoring the integrated H-atom signal, they have measured the excitation function of the $O(^1D) + H_2$ reaction and have proved the contribution of the PES of the electronically excited states whose participation is theoretically suggested.[50–53] Very recently, the reactive resonance structure[54] in the excitation function of F + HD reaction is also observed with this apparatus.[55] The observed resonance feature for the D + HF product channel and the non-resonance feature for the H + DF product channel are satisfactorily reproduced by quantum scattering calculations for this reaction.

Although the knowledge obtained in the study of chemical reaction dynamics becomes wider and finer, day by day, the present high-performance investigations do not necessarily deepens our understanding of chemical reaction dynamics. First, the currently undergoing rigorous comparisons between the experimental and theoretical results are limited to very simple triatomic systems.[40,42–45,51,52,55–57] Thus, our knowledge of chemical reaction dynamics for the reactions involving more than three atoms still remain ambiguous. From the feature of experimentally observed product-state distribution and DCS, the reactions are interpreted in terms of the prototype reaction mechanisms such as abstraction, stripping, insertion, or long-lived complex. Such phenomenological classification, however, does not help to obtain comprehensive understanding of chemical reaction dynamics. Furthermore, the classification of reaction mechanism only based on the product-state distribution and DCS does not reveal how the reaction proceeds on PES, for example, after the insertion. Second, the relation between energy randomization and dynamics on PESs needs to be carefully discussed. Generally, statistical energy disposal has been understood as the intramolecular energy redistribution in a reactive intermediate according to Fermi's Golden Rule. This means that the energy randomization is governed by the density of states of the vibrational modes of the reactive intermediate and the couplings among these modes. To discuss the statistical nature in the energy disposal, tetra-atomic systems are the smallest systems to yield two molecular products. However, reliable information of these factors is not easily obtained since reasonably accurate full-dimensional PESs have not been calculated except for triatomic systems. As a consequence, the existence of a deep potential well of the reactive intermediate has often been assumed as a practical criterion for discussing the statistical energy randomization in a particular reaction. This criterion is associated with the idea that reactive trajectories spend long time within a deep potential well to attain statistical energy randomization. However, the essential factor is a relative magnitude between the lifetime of the reactive intermediate and the time required for the energy randomization. Therefore, it should be emphasized that the experimental and theoretical knowledge to date does not reveal relative importance between the coupling strength and lifetime in the energy randomization for individual gas-phase chemical reactions.

In this account, we review our recent experimental studies on the stereodynamics of $O(^1D)$ and $O(^3P)$ atom reactions with simple molecules via polarized Doppler-resolved laser-induced fluorescence (LIF) spectroscopy. These reactions are known to play important roles in atmospheric chemistry[6] and combustion chemistry,[7] and thus have been extensively studied in microscopic dynamics as well as in their macroscopic rate constants.[58–60] However, most studies on the reaction dynamics of these reactions have been limited to product-state distribution measurements. The reaction dynamics speculated only from such scalar information contains significant ambiguities and thus has caused controversies in reaction mechanisms. As presented in Sec. I, the measurement of vector properties can solve such problems, since the angular correlations among the vectorial quantities contain direct and dynamic information during the course of chemical reactions. We have therefore measured the vector properties of these reactions on the rovibrational-state selected level, in particular, the correlated angular distributions among the velocity and rotational angular momentum vectors in bimolecular reactions. The analysis including the rotational angular momentum polarization of reaction products is important since it provides the information of torque to rotate the observed product species. Consequently, it is possible to discuss how the intermediate of the reaction deforms its structure to yield the products, and thus the reaction mechanism is deduced more directly than the previous studies. Furthermore, such information can be related to the difference in the degree of energy randomization. Although the current crossed molecular beam experiments have realized the high-resolution detection of scattering angle and product speed with sharply defined collision energies, the measurement of the rotational angular momentum polarization is difficult. Thus, the experiments measuring the correlated angular distribution are important to elucidate chemical reaction dynamics. In the present review, our attention is focused on the dominant and overall trends of the vector correlations rather than the minute details of its dependences on collision energies and product states. The fine structure of angular distribution and the fine state-dependence of the vector correlations must be pursued in the future when the sharp preparation of collision energy and the high-resolution measurement of the product velocity become possible.

This account is organized as follows. In Sec. I, we introduce the vector correlations in bimolecular reactions as well as experimental methods for measuring the vector properties. The details of the experimental setup and theoretical background necessary for the analysis are given in Secs. II and III, respectively. The review of the stereodynamics of O(^{1}D) and O(^{3}P) atom reactions is presented in Sec. IV. Section V closes this account with perspectives.

I. Vector Correlations in Bimolecular Reactions

The knowledge of product-state distribution gives an elementary picture of individual chemical reactions.[1–4] However, product-state distribution only shows the final outcome of the reaction and does not give direct information of the dynamics that yields such an outcome. For example, the origin of rotational motion of product molecules cannot be identified from the product-state distribution alone. This type of information is manifested only in the vectorial quantities of molecular fragmentation. To give a simple example, let us start with the application of vector correlations in photodissociation and then proceed to bimolecular reactions.

The important vectors to describe the stereodynamics in photodissociation are the transition dipole moment vector ($\boldsymbol{\mu}$) of the parent molecule, the recoil velocity vector ($\mathbf{v}$), and the rotational angular momentum vector ($\mathbf{j}$) of the photofragments [see Fig. 1(a)]. The angular correlations (or angular distributions) among these three vectors are called "vector correlations." As described below, the vector correlations are indispensable to obtain details of stereodynamics of photodissociation and thus have been extensively investigated.[61–64] One of the key points in measuring the vector correlations lies in the photoexcitation process. The spatial orientation of the parent molecules excited by linearly polarized light is anisotropic in the space-fixed laboratory (LAB) frame, since the probability of dipole transition is proportional to the cosine square of the angle between the electric vector and the transition dipole of the molecule. Thus, the spatial distribution of $\mathbf{v}$ and $\mathbf{j}$ can be anisotropic, and their degrees of anisotropy in the LAB frame represent the stereodynamics in the molecule-fixed frame. The angular correlation of $\mathbf{v}$ and $\mathbf{j}$ with respect to the linear polarization vector (electric vector) of the photolysis laser light, $\boldsymbol{\varepsilon}_\mathrm{p}$, are called $\boldsymbol{\mu}$–$\mathbf{v}$ correlation and $\boldsymbol{\mu}$–$\mathbf{j}$ correlation, respectively. In referring the $\boldsymbol{\mu}$–$\mathbf{v}$ and $\boldsymbol{\mu}$–$\mathbf{j}$ correlations, $\boldsymbol{\mu}$ is not a usual molecule-fixed vector, which rotates with a molecule. As shown in Fig. 1(a), $\boldsymbol{\mu}$ is a space-fixed vector defined as the direction of the transition dipole moment at the time of photoabsorption, $\boldsymbol{\mu}(t = 0)$, which has the cosine-square spatial distribution relative to $\boldsymbol{\varepsilon}_\mathrm{p}$.

(a) Vectors in photodissociation

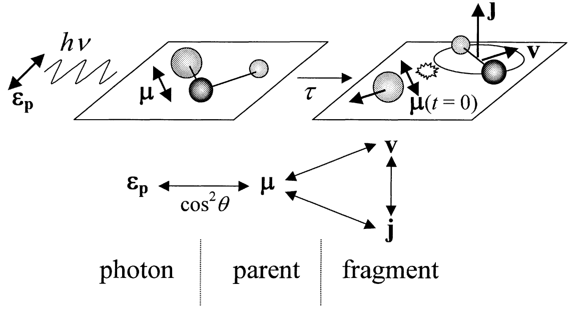

(b) Examples of $\mathbf{v}$–$\mathbf{j}$ correlation

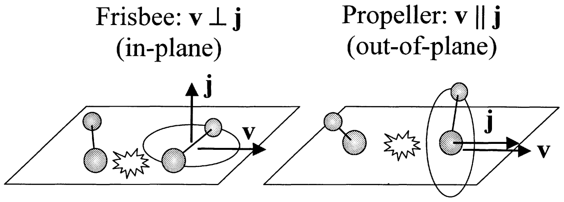

Fig. 1. (a) Vectors in photodissociation. A triatomic molecule is excited by laser light of energy $h\nu$ with the linear polarization $\boldsymbol{\varepsilon}_\mathrm{p}$. The excited molecule dissociates at $t = \tau$. The angular correlations among $\boldsymbol{\mu}$, $\mathbf{v}$, and $\mathbf{j}$, describe the stereodynamics of molecular photodissociation. In this case, the transition dipole moment $\boldsymbol{\mu}$ lies in the breaking bond. However, the excited parent molecule rotates before the dissociation and thus $\boldsymbol{\mu}(t = 0)$ do not coincide with $\mathbf{v}$. The diagram depicting the relation among $\boldsymbol{\varepsilon}_\mathrm{p}$ and $\boldsymbol{\mu}$–$\mathbf{v}$–$\mathbf{j}$ is taken from Ref. 62. (b) Examples of $\mathbf{v}$–$\mathbf{j}$ correlation: the "frisbee" type (in-plane torque) and the "propeller" type (out-of-plane torque).

For one-photon photodissociation with linearly polarized light, the spatial distribution of the recoil direction of photofragments is expressed as

$$f(\Theta_\mathrm{t}) = \frac{1}{4\pi}[1 + \beta P_2(\cos\Theta_\mathrm{t})], \tag{1}$$

where Θ_t is the recoil direction measured from $\boldsymbol{\varepsilon}_\mathrm{p}$ and $P_2(\cos\theta) = (3\cos^2\theta - 1)/2$ is the second order Legendre polynomial. The degree of anisotropy in the velocity distribution is characterized by the anisotropy parameter, $\beta(-1 \leq \beta \leq 2)$. If the dissociation occurs before the rotation of the parent molecule, β directly expresses the angular relation between the recoil velocity vector and the transition dipole moment vector in the molecule-fixed frame. By denoting this angle as χ, the β value of the prompt dissociation can be written as

$$\beta = 2\langle P_2(\cos\chi)\rangle. \tag{2}$$

Here $\langle\ldots\rangle$ represents the average over the angular distribution of χ. The rotation of the parent molecule blurs this clear angular relation [for example, in Fig. 1(a), $\boldsymbol{\mu}(t = 0)$ originally lies in the breaking bond but do not coincide with $\mathbf{v}$ due to the rotation before the dissociation]. The absolute value of β decreases down to one fourth of that of Eq. 2 for the infinitely long-lived case.[65] The angular distribution expressed as Eq. 1 can be detected by utilizing Doppler spectroscopy. In the Doppler spectroscopy, velocities are measured as Doppler shifts, which are proportional to the one-dimensional (1D) projection of $\mathbf{v}$ onto the propagation direction of the probe laser, $\mathbf{k_a}$. Suppose that all the photofragments have the same speed $v \equiv |\mathbf{v}|$. If the angular distribution is isotropic ($\beta = 0$), the photofragments uniformly distribute in a sphere of radius v. In this case, the 1D-projected speed, $v_{\rm 1D}$, continuously ranges $-v \le v_{\rm 1D} \le +v$, and the number density of molecules in an interval of $dv_{\rm 1D}$ is equal. As a consequence, the Doppler line shape is rectangle. In contrast, if the angular distribution is anisotropic ($\beta \neq 0$), the number density of molecules in an interval of $dv_{\rm 1D}$ depends on the angular distribution and the angle between $\boldsymbol{\varepsilon}_\mathbf{p}$ and $\mathbf{k_a}$, which is denoted as $\theta_{\rm a}$. The angular distribution is thereby translated into the Doppler line shape as a function of Doppler shift $\nu = (\nu_0\, v_{\rm 1D})/c$ (c: the speed of light):

$$D(\nu) = \frac{1}{2(\nu_0 v/c)}\left[1 + \beta P_2(\cos\theta_{\rm a})P_2\!\left(\frac{v_{\rm 1D}}{v}\right)\right], \tag{3}$$

where ν_0 is the line center frequency. The change of the Doppler line shape against $\theta_{\rm a}$ is schematically shown in Fig. 2(a): $D_{\parallel} \propto 1 + \beta P_2(v_{\rm 1D}/v)$ for $\boldsymbol{\varepsilon}_\mathbf{p} \parallel \mathbf{k_a}$ and $D_{\perp} \propto 1 - \beta P_2(v_{\rm 1D}/v)/2$ for $\boldsymbol{\varepsilon}_\mathbf{p} \perp \mathbf{k_a}$. If the photofragments are produced in a sharp single speed, the angular distribution characterized by β can be determined from a single Doppler profile. However, in most cases, photofragments are distributed in various speeds according to the energy partitioning among the photofragments. Since this distribution also affects the Doppler line shape, the measurement of Doppler profiles at two different geometries, such as $D_{\parallel}$ and $D_{\perp}$, is required to determine both the speed and angular distributions. One of the techniques to separately determine speed distribution and anisotropy is constructing "composite Doppler profiles" shown in Fig. 2(b). In addition to the Doppler spectroscopy measuring velocity in the frequency domain, the 1D projection of recoil velocity can be measured in the time domain as TOF spectra by ionizing the photofragments.[66,67] Furthermore, the distribution can be measured as two-dimensional (2D) projection with position-sensitive detection such as imaging method (see Fig. 2).[68,69]

(a) Detection of speed distribution and spatial anisotropy

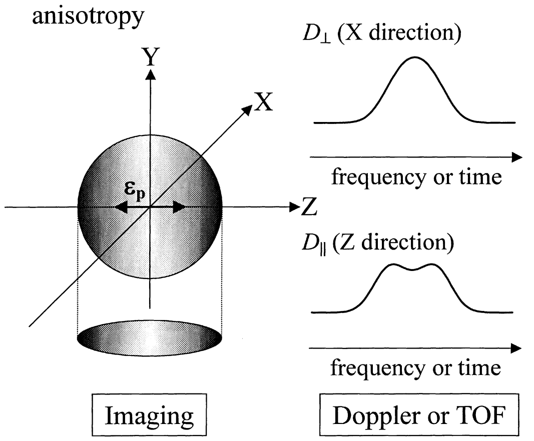

(b) Composite profiles

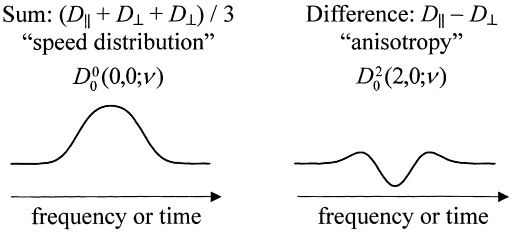

Fig. 2. (a) Detection of speed distribution and spatial anisotropy. The sphere represents the anisotropic spatial distribution of the photofragments. The electric vector of the photolysis light, $\boldsymbol{\varepsilon}_\mathbf{p}$, lies in the Z axis and the photofragments are assumed to be preferentially populated along this direction, corresponding to $\beta > 0$. In other words, the photofragments have a large v_Z component and small v_X and v_Y components. The Doppler profile, $D_\perp$, is obtained when the photofragments are detected with the probe laser propagating along the X (or Y) axis. The profile of $D_\perp$ is determined by the v_X (or v_Y) distribution and thus the small Doppler shifts are dominant. In contrast, $D_\parallel$ measures the v_Z distribution, where the large Doppler shifts are dominant. If the photofragments are ionized and all the ionized photofragments are detected, the time-domain profiles of TOF spectra are similar to the frequency-domain profiles of Doppler spectra. The spatial distribution can be observed as the 2D projection by utilizing the imaging method. (b) The examples of the "composite profiles." The anisotropic component is canceled in the sum of the Doppler profiles, $(D_\parallel + D_\perp + D_\perp)/3$, which expresses the isotropic component, i.e., "speed distribution." By contrast, the difference of the Doppler profiles, $D_\parallel - D_\perp$, only contains the anisotropic component.

As for rotational angular momentum, its spatial distribution is probed via the dependences of the rotational line intensities on the polarization of probe laser, $\boldsymbol{\varepsilon}_\mathbf{a}$.[31] The dependences are determined from the relation between the direction of the transition moments in electronic transitions and the plane of rotation (POR) of diatomic molecules; the transition moment, $\boldsymbol{\mu}'$, lies in the POR for P or R branch ($\boldsymbol{\mu}' \perp \mathbf{j}$), while the transition moment is perpendicular to the POR for Q branch ($\boldsymbol{\mu}' \parallel \mathbf{j}$). Thus, the orientation of POR in the LAB frame can be detected by measuring the line intensities with changing the angle between $\boldsymbol{\varepsilon}_\mathbf{p}$ and $\boldsymbol{\varepsilon}_\mathbf{a}$ or with changing the rotational branch. In the semiclassical expression,[70] the anisotropic distribution of rotational angular momentum is characterized by the rotational alignment, $A_0^{(2)}$: [31]

$$A_0^{(2)} = \langle P_2(\cos\Theta_{\rm r})\rangle, \tag{4}$$

where, $\Theta_{\rm r}$ is the angle between $\mathbf{j}$ and $\boldsymbol{\varepsilon}_\mathbf{p}$. The angular distribution of $\mathbf{j}$ also affects the profiles of Doppler, TOF, and imaging spectra. Accordingly, the expression of the Doppler profiles contains more terms than those appearing in Eq. 3. As a consequence, the Doppler profiles of LIF signal depend on the direction of polarization vector and that of propagation vector of the pump, probe and emitted photons. Dixon derived the formulation to analyze such complicated Doppler profiles with bipolar expansion of the correlated angular distribution among $\boldsymbol{\mu}$–$\mathbf{v}$–$\mathbf{j}$.[32] By utilizing Dixon's formulation, Docker showed that six Doppler profiles (three different geometries each for P or R branch and Q branch) are necessary to determine the speed distribution and the correlated angular distributions.[71] In this analysis, one needs to generate more sophisticated composite Doppler profiles than those shown in Fig. 2(b). The same technique is applied for the analysis of bimolecular reactions and the outline of such analyses is presented in Sec. III.

As described above, the $\boldsymbol{\mu}$–$\mathbf{v}$ and $\boldsymbol{\mu}$–$\mathbf{j}$ correlations represent the angular distributions relative to the space-fixed vector $\boldsymbol{\mu}(t = 0)$. Consequently, the $\boldsymbol{\mu}$–$\mathbf{v}$ and $\boldsymbol{\mu}$–$\mathbf{j}$ correlations are blurred by the rotation of the parent molecule following the photoexcitation. Thus, the $\boldsymbol{\mu}$–$\mathbf{v}$ and $\boldsymbol{\mu}$–$\mathbf{j}$ correlations contain the information of the lifetime of the parent molecule in the excited states. The absolute values of these correlations also depend on the angular relation between the molecule-fixed transition dipole moment and $\mathbf{v}$ or $\mathbf{j}$ [see Eq. 2 for $\boldsymbol{\mu}$–$\mathbf{v}$ correlation]. Since such angular relations in the molecule-fixed frame are not significantly complicated in most cases, the $\boldsymbol{\mu}$–$\mathbf{v}$ and $\boldsymbol{\mu}$–$\mathbf{j}$ correlations have been used to determine the type of transition and the symmetry of the excited states. Different from $\boldsymbol{\mu}$–$\mathbf{v}$ and $\boldsymbol{\mu}$–$\mathbf{j}$ correlations, the $\mathbf{v}$–$\mathbf{j}$ correlation represent the angular correlation purely defined in the molecule-fixed frame [see the diagram in Fig. 1(a)]. This correlation provides the information of the force generating the rotation of photofragments in the exit channel. In other words, how the parent molecule deforms its structure during the course of bond breaking. Figure 1(b) shows the two extreme cases in the $\mathbf{v}$–$\mathbf{j}$ correlation; the "frisbee" type ($\mathbf{v} \perp \mathbf{j}$) and the "propeller" type ($\mathbf{v} \parallel \mathbf{j}$). The frisbee case is caused by in-plane torque to rotate the photofragments, while the propeller type is the consequence of out-of-plane torque. Such information directly reflects the dynamics proceeding on the PESs.

For bimolecular reactions [see Fig. 3(a)], in place of the three-vector $\boldsymbol{\mu}$–$\mathbf{v}$–$\mathbf{j}$ angular correlation for molecular photodissociation, the fundamental angular correlations are those among the relative velocity vectors of reactants ($\mathbf{k}$) and products ($\mathbf{k}'$), and the product rotational angular momentum vector ($\mathbf{j}'$).[72–76] Figure 3(a) depicts the vectors in photoinitiated bimolecular reaction, where one of the reactants is generated from molecular photodissociation. In the center-of-mass (CM) frame of bimolecular reactions, $\mathbf{k}$ plays a similar role as $\boldsymbol{\mu}(t = 0)$ does in molecular photodissociation. The $\mathbf{k}$–$\mathbf{k}'$ correlation simply corresponds to the familiar quantity of DCS. As discussed in crossed molecular beam studies,[1,2] this correlation reflects the distribution of scattering angle, which is closely related to the reaction mechanism, opacity function, and lifetime of the collision complex. The $\mathbf{k}$–$\mathbf{j}'$ correlation represents the extent of the memory of the initial direction of the relative velocity vector. The $\mathbf{k}'$–$\mathbf{j}'$ correlation reflects the torque on the product molecules, just like the $\mathbf{v}$–$\mathbf{j}$ correlation in photodissociation. The angular distribution of $\mathbf{j}'$ vector relative to the $\mathbf{k}$–$\mathbf{k}'$ collision plane describes how strongly the molecular plane of the reactive intermediate remains coincident to the collision plane during the reaction and how the reactive intermediate changes its molecular structure relative to that plane.

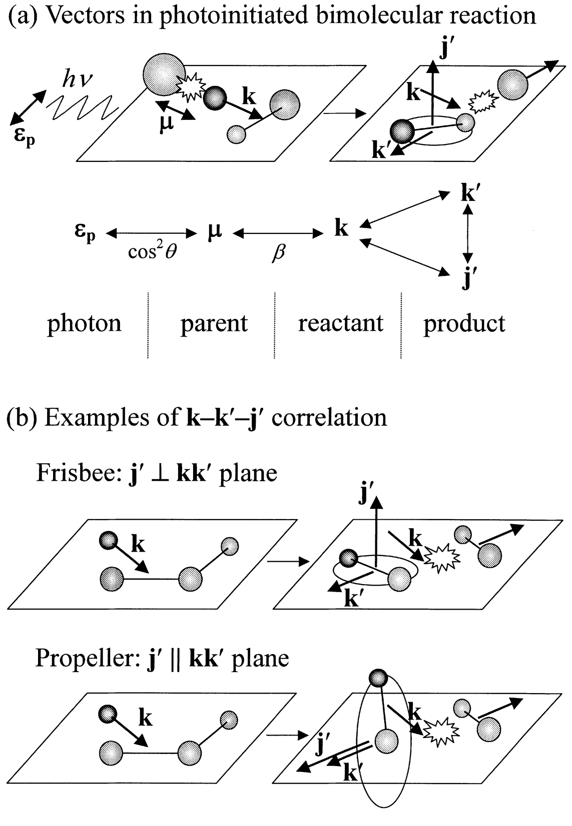

Fig. 3. (a) Vectors in photoinitiated bimolecular reactions. A precursor molecule is excited by laser light of energy $h\nu$ with the linear polarization $\boldsymbol{\varepsilon}_p$. The excited molecule dissociates and one of the fragments reacts with another reactant molecule. The angular correlations among $\mathbf{k}$, $\mathbf{k}'$, and $\mathbf{j}'$, describe the stereodynamics of bimolecular reactions. Note that the $\mathbf{k}$ vector acts as the similar role of $\boldsymbol{\mu}$ in molecular photodissociation shown in Fig. 1(a). Although these figure and diagram indicate that the $\mathbf{k}$–$\mathbf{k}'$–$\mathbf{j}'$ correlation can be directly related to $\boldsymbol{\varepsilon}_p$ and $\boldsymbol{\mu}$, in fact, the product velocity is not measured as $\mathbf{k}'$ in the CM frame but as $\mathbf{v}'$ in the LAB frame. Thus, the appropriate coordinate transformation is required in the analysis. (b) Two extreme examples of $\mathbf{k}$–$\mathbf{k}'$–$\mathbf{j}'$ correlation: the "frisbee" type (in-plane torque) and the "propeller" type (out-of-plane torque).

The angular correlations among the $\mathbf{k}$–$\mathbf{k}'$–$\mathbf{j}'$ vectors can be extracted from the Doppler analysis as performed in photodissociation studies. The key point to measure the CM $\mathbf{k}$–$\mathbf{k}'$–$\mathbf{j}'$ angular correlation with the Doppler spectroscopy is the observation of the LAB velocity. The basic principle is schematically shown in Fig. 4, for A + BCD → AB + CD reaction, where the product AB is scattered with the recoil velocity $\mathbf{w}_{\mathrm{AB}}$ in the CM frame. If the product AB is scattered into the same direction as $\mathbf{k} = \mathbf{w}_{\mathrm{A}} - \mathbf{w}_{\mathrm{BCD}}$ ($\theta_t < 90°$: forward scattering), its LAB speed, $v_{\mathrm{AB}} \equiv |\mathbf{v}_{\mathrm{AB}}|$, is larger than $w_{\mathrm{A}} \equiv |\mathbf{w}_{\mathrm{A}}|$. In contrast, v_{AB} is smaller than w_{A} for backward scattering ($\theta_t > 90°$). Thereby,

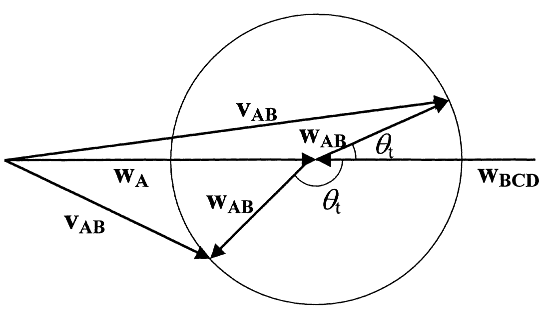

Fig. 4. The basic principle to determine the CM scattering angle by measuring the LAB velocity. The reaction of A + BCD → AB + CD is assumed.

the scattering angle in the CM frame can be measured as the LAB speed v_{AB}. In general, AB products are scattered with various $w_{AB} \equiv |\mathbf{w}_{AB}|$ according to the internal energy distribution of the sister fragments CD and the spread of collision energies. Accordingly, in addition to v_{AB}, the angle between $\mathbf{w}_A$ and $\mathbf{v}_{AB}$ is necessary to specify θ_t and w_{AB}. The information of this angle can be obtained if the LAB frame distribution of $\mathbf{v}_A$ is anisotropic. In the photoinitiated reaction experiments shown in Fig. 3(a), a linearly polarized photolysis (pump) laser light generates the anisotropic distribution of the reactive species A, which is characterized by β [see Eq. 1]. Thus, without using crossed molecular beam apparatus, the *photo*initiated reaction determines the CM distribution of θ_t and w_{AB} from the LAB speed distribution and anisotropy of the products, based on the *law of cosines* as called the "photoloc" method.[77,78] The products are probed with a polarized laser light, and then the angular distribution of $\mathbf{j}'$ in the CM frame is analyzed, as in the photodissociation studies. In fact, the relation between the CM velocities and the LAB velocities is not so simple as shown in Fig. 4. The relation between $\mathbf{v}$–$\mathbf{v}'$–$\mathbf{j}'$ and $\mathbf{k}$–$\mathbf{k}'$–$\mathbf{j}'$ vectors are shown in Fig. 5. Here, $\mathbf{v} \equiv \mathbf{v}_1$ is the LAB frame velocity vector of the reactant which carries the anisotropy produced in the photolysis by the pump laser. The detail of the connection between these vectors is presented in Sec. III.

In the pump-probe experiments, the rotational angular momentum polarization of bimolecular reaction products was first reported by Kleinermanns et al. for H + O_2 reaction in 1985.[79,80] They measured $A_0^{(2)}$ and observed a strong rotational angular momentum polarization of OH products perpendicular to the incident velocity vector of the H atom in the LAB frame. Almost a decade later, Hall and coworkers analyzed the Doppler profiles of the OH products of this reaction with taking account of the correlated angular distribution of $\mathbf{k}$–$\mathbf{k}'$–$\mathbf{j}'$.[81] They first demonstrated the power of the analysis using basis functions to fit Doppler profiles. Although their analysis fixed the angular distributions of $\mathbf{j}'$ relative to $\mathbf{k}'$ at simple limiting cases, sophisticated general analyses of the three-vector $\mathbf{k}$–$\mathbf{k}'$–$\mathbf{j}'$ correlation in bimolecular reactions were developed in the middle 1990's.[78,82–84] Based on these methods for the data analysis, experimental studies have been undertaken by Simons–Brouard's group[85–95] and Hancock's group,[86,96,97] both in Oxford, Hall's group in Brookhaven,[81,98] Zare's group in Stanford,[99,100] and the authors in Kyoto.[101–105] In Oxford, Brookhaven, and Kyoto, the polarized Doppler LIF method is utilized, while the Stanford group have adopted the core-extraction method[106] in resonance-enhanced multiphoton ionization (REMPI) detection.[107]

(a) CM frame: $\mathbf{k}$–$\mathbf{k}'$–$\mathbf{j}'$

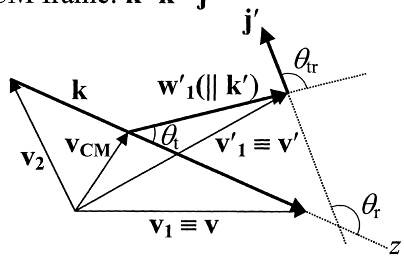

(b) v_1 frame: $\mathbf{v}$–$\mathbf{v}'$–$\mathbf{j}'$

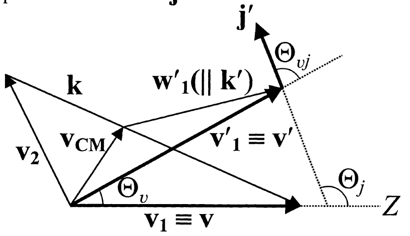

Fig. 5. The relation between the $\mathbf{k}$–$\mathbf{k}'$–$\mathbf{j}'$ vectors in the CM frame and the $\mathbf{v}$–$\mathbf{v}'$–$\mathbf{j}'$ vectors in the v_1 frame. Here, $\mathbf{v} \equiv \mathbf{v}_1$ is the velocity vector of the reagents produced by the photodissociation and $\mathbf{v}_2$ is that of another reactant molecule. The vectors $\mathbf{w}'_1$ and $\mathbf{v}'_1$ represent the velocity of the product which contains the reagent species associated with $\mathbf{v}_1$, in the CM frame and the LAB frame, respectively. Note that $\mathbf{w}'_1$ is not necessarily lies in the $\mathbf{v}_1$–$\mathbf{v}_2$ plane.

There are three limiting prototypes for the polarization of $\mathbf{j}'$ relative to $\mathbf{k}$ and $\mathbf{k}'$: the "frisbee" type for $\mathbf{j}' \perp \mathbf{k}$ and $\mathbf{j}' \perp \mathbf{k}'$ (consequently $\mathbf{j}' \perp \mathbf{k}$–$\mathbf{k}'$ plane), the "cartwheel" type for $\mathbf{j}' \perp \mathbf{k}'$ and $\mathbf{j}'$ in $\mathbf{k}$–$\mathbf{k}'$ plane, and the "propeller" type for $\mathbf{j}' \parallel \mathbf{k}'$ (consequently $\mathbf{j}'$ in $\mathbf{k}$–$\mathbf{k}'$ plane). The frisbee case is observed when the intermediate (not always meaning long-lived) rotates in the $\mathbf{k}$–$\mathbf{k}'$ scattering plane and in-plane bending motions exert a torque on the product rotation [see Fig. 3(b)]. On the other hand, the propeller case originates from the out-of-plane torsional force and products recoil along the axis of this force [see Fig. 3(b)]. The cartwheel case is rather complex and, for example, bending (not torsional) motions out of the scattering plane act as a torque on the product rotation. In this way, the dynamics on the PESs is directly elucidated from the vector information.

The correlated angular distributions of $\mathbf{k}$–$\mathbf{k}'$–$\mathbf{j}'$ have been studied for simple gas phase elementary reactions and have provided the direct information of reaction dynamics as reviewed below. Some of the reactions showed different angular correlations between the two Λ-doublet components[108] of the $^2\Pi$ states of the products, $\Pi(A')$ and $\Pi(A'')$.[109] The origin of such differences is not clearly solved yet and thus only the results are mentioned here. In the H + O_2 reaction, Hall and coworkers found that the OH products in the $\Pi(A')$ Λ-doublet levels were polarized ($\mathbf{j}' \perp \mathbf{k}'$) whereas the $\Pi(A'')$ Λ-doublet levels were isotopic.[81,98] Brouard et al. showed polarized $\Pi(A')$ of cartwheel type and isotropic $\Pi(A'')$ for OH products in $O(^1D)$ + CH_4 reaction[90] and, conversely, OH products were polarized for $\Pi(A'')$ and much less polarized for $\Pi(A')$ in H + CO_2 reaction.[92] They found frisbee-type $\Pi(A')$ and cartwheel-type $\Pi(A'')$ for $O(^1D) + H_2$ reaction.[93] In contrast to these reactions, the Λ-doublet dependence of the rotational polarization of the OH products was not observed for $O(^3P) + H_2S$ reaction studied by Hancock and coworkers.[97] The observed frisbee-type OH rotational angular momentum polarization indicated the planer transition state of OHSH. In the recent Doppler studies for the OH products of $H + N_2O$ (Ref. 94) and $H + CO_2$ (Ref. 95) reactions, Brouard et al. have shown that $\mathbf{j'}$ lies in the $\mathbf{k}$–$\mathbf{k'}$ scattering plane, i.e., $\mathbf{j'} \parallel \mathbf{k'}$. This propeller-type correlation reflects the dominance of the out-of-plane torsional motion in HONN and HOCO intermediates. The possibility of torsional excitation in their exit channels is speculated from the orbital symmetry and the analogy with the dynamics observed in the first electronically excited state of isoelectronic system of HN_3.[94,95] Zare and coworkers measured the rotational angular momentum polarization of the HCl products in $Cl + CH_4$ and $Cl + C_2H_6$ reactions.[99,100] The magnitude and the trend of the rotational polarization strongly depend on the reactant species, rovibrational levels of products, and isotopic variants (H or D). In the $Cl + CH_4$ reaction,[99] only the $HCl(v' = 1, j' = 1)$ products show a large rotational alignment $\mathbf{j'} \parallel \mathbf{k'}$. Since the forward scattered component is dominant for this channel, the H-atom abstraction mechanism is proposed. In this mechanism, the line-of-centers force is considered to act as the torque to rotate the $HCl(v' = 1, j' = 1)$ products in the transfer of the H atom from C to Cl at the closest approach. Similar rotational polarization is observed for $DCl(v' = 0, j' = 1)$ products in $Cl + C_2D_6$ reaction while $DCl(v' = 0, j' = 1)$ products in $Cl + CD_4$ reaction show strong $\mathbf{j'} \perp \mathbf{k'}$ correlation.[100] This difference is interpreted in terms of the location of the D-atom transfer along the reaction coordinate: the early transfer near the closest approach for the $Cl + C_2D_6$ reaction and the late transfer for the $Cl + CD_4$ reaction.

The brief review presented above is focused on the studies measuring rotational angular momentum polarization in bimolecular reactions. In addition to these studies, similar measurements probing molecular products have been performed for various bimolecular reactions, although the rotational polarization analyses have not been undertaken. The reactions studied so far with the Doppler-resolved LIF method, mostly by the Oxford, Brookhaven, and Kyoto groups,[105] are $O(^1D) + N_2O$,[85–87,103] $O(^1D)$ + hydrocarbons,[88–90,93,101,104,110] $O(^1D) + HCl$,[91] $O(^1D) + H_2$,[93,111,112] $O(^1D) + H_2O$,[102,113] $H + O_2$,[79–81,98] $H + CO_2$,[92,95,114] $H + H_2O$,[115,116] $H + N_2O$,[94,117,118] $H + H_2S$,[119] $O(^3P) + CS$,[86,96] $O(^3P) + H_2S$,[97] and $O(^3P)$ + hydrocarbons[120] reactions. The Stanford group has studied Cl atom reactions with H_2 (Ref. 57) and hydrocarbons[99,100,121–126] and $H + H_2$ reaction[127–130] via REMPI detection, mostly with the core-extraction method.

Before closing this section, we discuss about the merits and demerits among the experimental techniques for investigating stereodynamics. Such comparison clarifies the reason why we adopted the Doppler LIF method as well as the limitation of this method. As for the limitation, its drawback to the present studies and what is desired in the next stage are presented in Sec. V. As reviewed in the beginning of this account, for the detailed measurement of DCS, the current trend is to utilize the high-resolution velocity mapping of reaction products. The velocity mapping is made possible with detection techniques such as ion imaging,[131] core extraction,[106] Rydberg tagging,[41] or Doppler-selected TOF.[49] All these ionization methods can select the velocity components of the ionized or tagged products in the space, time, or frequency domain; thereby the product velocities are measured with 2D or three-dimensional (3D) resolution. In most of these methods, detection of the high-speed H-atom products is the key point to resolve the rovibrational states of sibling molecular products. Their applicability is therefore limited to the reactions yielding the H-atom product. Another essential point to achieve the high resolution in product velocity is well-defined collision energies realized by a crossed molecular beam apparatus or the jet-coexpansion method.[121] In contrast, the LIF method is difficult to observe the products in the space-resolved manner by using the crossed molecular beam apparatus or imaging devices. This is due to the low sensitivity of the fluorescence detection, although a challenging attempt of LIF imaging of molecular products has been applied to the $B + O_2$ reaction by Chen and coworkers.[132] Thus, the LIF method measures the 3D-velocity distribution of the products via the Doppler shift, which is the 1D projection on the propagation direction of the probe laser light [see Fig. 2(a)]. In fact, Doppler line shapes are measured as the convolution of the product speed distribution $f(v)$ and the 1D-projected Doppler profile for each v. As described above, the 1D-projected speed v_{1D} of the molecules of speed v ranges $-v \leq v_{1D} \leq +v$. Thus, all the products with speed $v \geq |v_{1D}|$ contribute to the LIF signal at the Doppler shift $\nu = (\nu_0\, v_{1D})/c$. Accordingly, the velocity resolution of the 1D method is not so high as the 2D and 3D techniques, where the congestion of the signals with different v is not significant. As a consequence, it is difficult for 1D method to discuss about the dynamics sharply dependent on the rovibrational levels of sister products. As for this demerit, if the absorption of the products is strong enough, high-resolution transient frequency modulated absorption spectroscopy[133] can provide the differential form of the 1D-Doppler spectrum and thus the resolution can be improved. Another disadvantage in the Doppler experiment performed under a bulb condition is the difficulty in generating sharply defined collision energies since the translational energy of the one of the reactive species produced by photodissociation process cannot be arbitrarily controlled. In addition, if the kinematic condition is unfavorable, the thermal motions of reagents causes a substantial spread in collision energy distribution.[134] We will discuss whether this effect is serious or not for our studies, in Secs. IV and V.

In spite of the demerits noted above, the versatility of the fluorescence technique to detect fluorescent products is invaluable to study the important gas-phase elementary reactions. The OH radical is one of the typical products in such reactions, but is extremely difficult to be ionized by REMPI method.[135] Since we are most interested in the elementary reactions of oxygen atoms which play the important roles in the various fields of chemistry,[3,6,7] we select the LIF method to study the detailed stereodynamics of oxygen-containing reactions of fundamental importance. The most important thing is that the determination of the rotational angular momentum polarization is only possible via the detection of molecular products. Here, the determination of the rotational angular momentum polarization of product molecules does not mean the subtle "quantitative" measurement of a detailed distribution of magnetic sublevel of $\mathbf{j}'$. This information is used for a “qualitative” understanding of the bimolecular reactions, especially, via the forces acting in reactive intermediates. The H-atom detection in the high-resolution technique can never probe the rotational polarization of the sibling molecular products. The detection of molecular products with rovibrational-state selection reduces the signal intensity, since hundreds or thousands of molecular quantum states are generated in a reaction. This reduction makes the current high-resolution *crossed molecular beam* techniques unfavorable to universally apply for bimolecular reactions. In contrast, *low-pressure flow condition* of the Doppler LIF experiment provides a rather high molecular density, which allows the fine analysis including the rotational angular momentum polarization. As described here, to probe the rotational angular momentum polarization with the Doppler LIF method, lowering of the velocity resolution and averaging of the collision energies are inevitable. Thus, the results obtained in this method and those obtain in the crossed molecular beam experiments need to complement each other.

II. Experiment

Experimental setup is briefly described here, since the details were given elsewhere.[102] A typical apparatus is schematically depicted in Fig. 6(a). A mixture of precursor species for oxygen atom production [N_2O for $O(^1D)$ and NO_2 for $O(^3P)$] and reagent species (hydrocarbons, N_2O, or H_2O vapor) was introduced into the reaction chamber and continuously pumped with a rotary pump. In most experiments, the partial pressures of precursor and reactant species were set equal, about 100 mTorr, except for H_2O which was kept at 50 mTorr. The electronically excited oxygen atom, $O(^1D)$, was produced by the photodissociation of N_2O with 193 nm light. The atomic oxygen, $O(^3P)$, was prepared by the photodissociation of NO_2 at 308 nm and 351 nm to alter the collision energies. At a time delay of 100 ns after the photolysis laser radiation, tunable UV light was introduced into the reaction chamber to probe the nascent product $OH(v' = 0, 1, \text{and } 2)$ or $NO(v' = 0)$ by utilizing LIF via their $A^2\Sigma^+ - X^2\Pi$ excitation. Measurements of the Doppler profiles were performed with a dye laser equipped with an intracavity etalon. The line shape of the UV laser light was confirmed as Gaussian by measuring the Doppler profiles of thermally relaxed OH or NO products at the delay time longer than 10 μs. The deduced bandwidth of the probe UV light in the full width at half maximum (FWHM) was 0.04 cm^{-1} for the fundamental wave and 0.12–0.14 cm^{-1} for the second harmonic wave. The bandwidth of the probe laser is sufficient to analyze the trends of the vector correlations since the full widths of the observed Doppler profiles are typically 0.6–0.8 cm^{-1}, which correspond to the LAB speeds of the products $\approx$ 3000 m/s. However, the Doppler profiles of the OH products of the $O(^3P)$ reactions are narrow to analyze the polarization of rotational angular momentum. Total pressure and the pump-probe delay time were carefully chosen to minimize the effect of collisions, which change the magnitude and direction of both $\mathbf{v}'$ and $\mathbf{j}'$. We confirmed that the decrease of total pressure and pump-probe delay time from the conditions described above did not yield any appreciable changes in the Doppler line shapes within experimental errors. Moreover, we ensured that the probe laser power was weak enough to avoid the saturation effect[136] in the excitation process of the LIF detection.

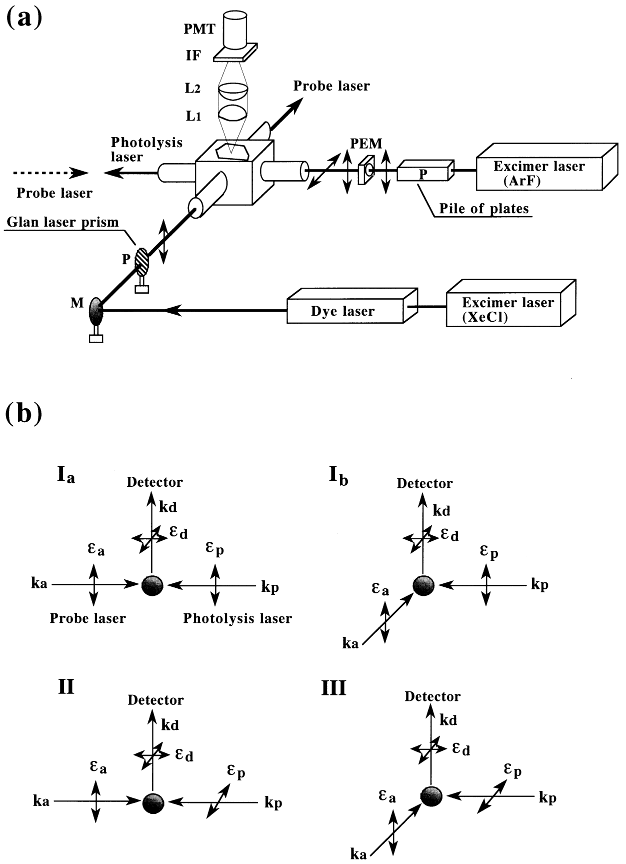

Fig. 6. (a) Schematic diagram of the experimental apparatus used for the measurement of Doppler profiles. M: mirror; P: polarizer; PEM: photoelastic modulator; L_i: synthetic silica Lens; IF: interference filter; and PMT: photomultiplier tube. The probe laser beam was introduced into the vacuum chamber either collinearly or orthogonally to the photolysis laser beam. (b) The LIF excitation-detection geometries employed in the measurement of Doppler profiles. The vectors $\mathbf{k}$ and $\boldsymbol{\varepsilon}$ represent the propagation vectors and electric vectors, respectively, for the laser light or fluorescence. The subscripts p, a, and d denote the photolysis, absorbed, and detected photons, respectively. Note that the geometries I_a and I_b are equivalent. As shown here, only the geometries with $\boldsymbol{\varepsilon}_a \parallel \mathbf{k}_d$ are used in the analysis and the fluorescence is detected without polarizer to generate useful composite Doppler profiles.[71]

The fluorescence from OH(A) or NO(A) was viewed from the direction perpendicular to both the photolysis and probe laser beam axes. Appropriate filters were placed in front of the photomultiplier tube to eliminate the strong scattered light and emission arising from the photolysis and probe lasers. The repetition rate of the experiments was 10 Hz and each laser power was monitored by a photodiode for normalizing the LIF signal to correct for the fluctuations of the laser power.

As described in Sec. III, the shape of a Doppler profile contains the combined information of the correlated angular distributions among $\mathbf{k}$, $\mathbf{k}'$, and $\mathbf{j}'$. The contribution of each correlation to the Doppler profile depends on the direction of the polarization vector and that of propagation vector of the pump laser, probe laser, and emitted photon. Doppler-resolved spectral line profiles were measured in the three different LIF excitation-detection geometries: I, II, and III, depicted in Fig. 6(b). These geometries of $\boldsymbol{\varepsilon}_{\mathbf{a}} \parallel \mathbf{k}_{\mathbf{d}}$ are convenient to extract the vector properties of the Doppler-probed species, as shown by Docker.[71] To prepare these excitation-detection geometries, incomplete linear polarization of the UV probe light was converted to a high vertical polarization (degree of polarization > 0.99) with a Glan laser prism and a half-wave plate. The originally unpolarized ArF laser light was passed through a pile of plates consisting of twelve Brewster's angle quartz plates to obtain vertically polarized light (degree of polarization > 0.95). Shot-by-shot alternation of the polarization vector by utilizing a photoelastic modulator allows us to observe the two polarization-dependent spectral line profiles in the LIF geometries of $\mathrm{I_b}$ and III in a single scan. In order to improve the signal-to-noise ratio, 50–100 laser shots were averaged at each step of a frequency scan and the spectra obtained from 9–25 scans were summed up. For the $\mathrm{O(^3P)}$ production, the unpolarized XeCl or XeF laser light was passed through a Glan laser prism to yield a vertically polarized light (degree of polarization $>$ 0.99) instead of the pile of plates for the ArF laser light.

III. Analysis

As noted in Sec. I, the velocity measured in the Doppler spectroscopy is the LAB velocity ($\mathbf{v}'$) and is not the CM velocity ($\mathbf{k}'$). To extract the information of the scattering dynamics in the CM frame from the Doppler profiles in the LAB frame, Aoiz et al. developed a theoretical basis for the analysis.[82,83] This method connects the Dixon's formulation treating the vector correlations in molecular photodissociation[32] and a spherical harmonic expansion of the CM angular momentum distribution in bimolecular reactions, which was proposed by Shafer-Ray et al.[78] The great ability of this method to analyze DCS and rotational angular momentum polarization in bimolecular reactions has been successfully demonstrated and thus we adopted their formulation in the present study. In line with Ref. 83 but with slight modification in the notation, this section presents the outline of the Doppler analysis.

A. The k–k′–j′ Angular Distribution and the Bipolar Expansion. The CM coordinate system is shown in Fig. 7. The z axis of the CM frame lies in $\mathbf{k}$, and the polar angles of $\mathbf{k}$–$\mathbf{k}'$ and $\mathbf{k}$–$\mathbf{j}'$ are $\omega_\mathrm{t} \equiv (\theta_\mathrm{t}, \phi_\mathrm{t})$ and $\omega_\mathrm{r} \equiv (\theta_\mathrm{r}, \phi_\mathrm{r})$, respectively. The goal of the analysis is to obtain the correlated angular distribution function in the CM frame, $P(\omega_\mathrm{t}, \omega_\mathrm{r})$. The angular distribution of $\mathbf{k}$–$\mathbf{k}'$ and $\mathbf{k}$–$\mathbf{j}'$ are independently described by using the spherical harmonics, $Y_{k_1q_1}(\theta_\mathrm{t}, \phi_\mathrm{t})$ and $Y_{k_2q_2}(\theta_\mathrm{r}, \phi_\mathrm{r})$, respectively. Thus, the correlated angular distribution can be represented by utilizing the expansion with the product of these spherical harmonics, i.e., bipolar harmonics, $B_Q^K(k_1, k_2; \omega_\mathrm{t}, \omega_\mathrm{r})$.[137] In fact, the bipolar harmonics are constructed from the product of the modified spherical harmonics, $C_{kq}(\theta, \phi) \equiv [(2k + 1)/(4\pi)]^{1/2}\, Y_{kq}(\theta, \phi)$, as[137]

$$B_Q^K(k_1, k_2; \omega_\mathrm{t}, \omega_\mathrm{r}) = \sum_{q_1, q_2} (-1)^{K-Q} \sqrt{2K + 1} \begin{pmatrix} k_1 & K & k_2 \\ q_1 & -Q & q_2 \end{pmatrix} \times C_{k_1q_1}(\theta_\mathrm{t}, \phi_\mathrm{t}) C_{k_2q_2}(\theta_\mathrm{r}, \phi_\mathrm{r}), \tag{5}$$

where (: : :) is a 3–j symbol. The bipolar harmonics form an orthonormal complete set in the (ω_t, ω_r) space and thus the coefficients in the bipolar expansion are the expectation value of $P(\omega_\mathrm{t}, \omega_\mathrm{r})$ for $B_Q^K(k_1, k_2; \omega_\mathrm{t}, \omega_\mathrm{r})$. The expectation values are called the bipolar moments, $B_Q^K(k_1k_2)$,[138] and these moments characterize the correlated angular distribution. Dixon formulated the relation between Doppler profiles and the bipolar moments obtained for the LAB velocity.[32] Thus, the bipolar moments in the v_1 frame [Fig. 5(b)] rather than in the CM frame [Fig. 5(a)] are convenient to analyze the Doppler profiles. The CM angular distribution $P(\omega_\mathrm{t}, \omega_\mathrm{r})$ can be obtained form the bipolar moments in the v_1 frame with the appropriate coordinate transformation.

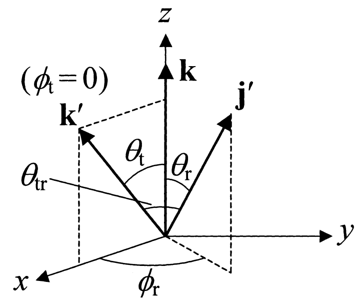

Fig. 7. The CM frame defining $\mathbf{k}$, $\mathbf{k}'$, and $\mathbf{j}'$ vectors. The initial relative velocity vector, $\mathbf{k}$, is defined as z axis. The solid angles $\omega_\mathrm{t} \equiv (\theta_\mathrm{t}, \phi_\mathrm{t})$ and $\omega_\mathrm{r} \equiv (\theta_\mathrm{r}, \phi_\mathrm{r})$ represents the direction of the final relative velocity vector $\mathbf{k}'$ and product rotational angular momentum vector $\mathbf{j}'$, respectively, with respect to $\mathbf{k}$. The $\mathbf{k}'$ vector lies in xz plane by putting $\phi_\mathrm{t} = 0$.

B. Doppler-Resolved Line Profiles. In case of the linearly polarized pump-probe experiment, the 1 + 1 LIF Doppler profile, $D(\nu)$, is symmetric with respect to the line center frequency ν_0 as shown in Fig. 2(a). The profile can be written by the Legendre polynomial expansion of $P_n(v_\mathrm{p}/v')$ of even order up to $n = 6$ since three photons are involved in the pump-probe-emission process. Here, $v_\mathrm{p} = |(\nu/\nu_0)c|$ represents the minimum product LAB velocity giving the displaced frequency ν as the Doppler shift. The integration over the product speed with the distribution function $f(v')$ yields the Doppler spectrum $D(\nu)$:[83]

$$D(\nu) = \int_{v_p}^{\infty} \frac{1}{2(\nu_0 v'/c)} \left[g_0(v') + g_2(v') P_2\!\left(\frac{v_\mathrm{p}}{v'}\right) \right] f(v') v'^2 \mathrm{d}v' \tag{6}$$

Here, the small contribution of $P_4(v_\mathrm{p}/v')$ and $P_6(v_\mathrm{p}/v')$ terms are neglected. The observed profiles are convolution of Eq. 6 and the band profile of a probe laser. Based on the semiclassical treatment[70] formulated by Dixon,[32] the coefficients $g_0(v')$ and $g_2(v')$ in Eq. 6 are expressed as[83]

$$g_0(v') = b_0 \overline{\beta_0^0(0, 0; v')} + b_1 \frac{\beta}{2} \overline{\beta_0^2(0, 2; v')} \tag{7}$$

and

$$g_2(v') = b_2 \frac{\beta}{2} \overline{\beta_0^2(2, 0; v')} + b_3 \overline{\beta_0^0(2, 2; v')} + b_4 \frac{\beta}{2} \overline{\beta_0^2(2, 2; v')}, \tag{8}$$

where β is the translational anisotropy parameter of the atomic reagent produced from the photodissociation of a molecular precursor. The $\overline{\beta_Q^K(k_1, k_2; v')}$'s in Eqs. 7 and 8 are the v_1 frame bipolar moments, which represent the vector correlations in the v_1 frame as a function of product LAB speed v'. The bar of $\overline{\beta_Q^K(k_1, k_2; v')}$ denotes the average of the bipolar moment in the v_1 frame, $B_Q^K(k_1, k_2; v', v_1, v_2)$, obtained by integrating all the possible velocities of the reagents, $\mathbf{v_1}$ and $\mathbf{v_2}$, in their magnitude and relative orientation. In Eqs. 7 and 8, if the factor $\beta/2$ is included in the bipolar moments, the moments are equivalent to those in the LAB frame. The multipliers b_i of bipolar moments in g_0 and g_2 depend on the LIF excitation geometries shown in Fig. 6(b) and the rotational branch in the probed transitions.

As described below, the indices K, Q, k_1, and k_2 represent the angular dependence of the correlated distribution, and thus the physical meaning of each moment is clear if one recognizes the meaning of the indices. The bipolar moments in the v_1 frame are the expectation value of the bipolar harmonics in the v_1 frame $B_Q^K(k_1, k_2; \Omega_v, \Omega_j)$, where, $\Omega_v \equiv (\Theta_v, \Phi_v)$ and $\Omega_j \equiv (\Theta_j, \Phi_j)$ are the angles of $\mathbf{v'}$ and $\mathbf{j'}$ with respect to $\mathbf{v_1}$ [see Fig. 5(b)]. The bipolar harmonics $B_Q^K(k_1, k_2; \Omega_v, \Omega_j)$ are constructed from $C_{k_1q_1}(\Theta_v, \Phi_v)C_{k_2q_2}(\Theta_j, \Phi_j)$ in the v_1 frame as those in the CM frame shown in Eq. 5. Here, k_1 and q_1 represent the angular dependence of $\mathbf{v'}$, while k_2 and q_2 represent that of $\mathbf{j'}$. The indices K and Q express the angular dependence of the correlated angular distribution specified both by the k_1 and k_2. As shown in Eq. 5, the K and Q arise in summing up q_1 and q_2 with a 3–j symbol and thus they are determined as the same way in the addition of angular momentum vectors $|k_1\, q_1\rangle$ and $|k_2\, q_2\rangle$, i.e., $|k_1 - k_2| \le K \le k_1 + k_2$ and $Q = q_1 + q_2$. For the linear polarization photolysis experiment, only $K = 0$ and $K = 2$ appear in the bipolar expansion and Q is restricted to zero ($Q = 0$ is the consequence of cylindrical symmetry). In addition, if the photoinitiated reaction process is non-chiral, k_1 and k_2 are limited to even values only. Since g_0 and g_2 are associated with $k_1 = 0$ and 2, respectively, the bipolar moments shown in Eqs. 7 and 8 are all the moments to be determined. As recognized from the angular dependence of spherical harmonics, $K = 0$ or $k_i = 0$ ($i = 1, 2$) corresponds to an isotropic component while $K = 2$ or $k_i = 2$ corresponds to an anisotropic component. Thus, the angular correlation corresponding to the v_1 frame bipolar moments $\beta_Q^K(k_1, k_2; v')$ can be summarized as follows (here, the arguments v_1 and v_2 are omitted for simplicity): $\beta_0^0(0, 0; v') = 1$ (population), $\beta_0^2(2, 0; v') = P_2(\cos \Theta_v)$, $\beta_0^2(0, 2; v') = P_2(\cos \Theta_j)$, and $\beta_0^0(2, 2; v') = P_2(\cos \Theta_{vj})$, where Θ_{vj} is the angle between $\mathbf{v'}$ and $\mathbf{j'}$ [see Fig. 5(b)]. The $\beta_0^2(2, 2; v')$ moment represents the $P_2(\cos \Theta_{vj})$ dependent both on the $P_2(\cos \Theta_v)$ and $P_2(\cos \Theta_j)$. The $\beta_0^2(2, 2; v')$ moment takes a positive value when two of the $\mathbf{v}$, $\mathbf{v'}$ and $\mathbf{j'}$ are parallel, while it takes a negative value when $\mathbf{v}$, $\mathbf{v'}$ and $\mathbf{j'}$ are parallel all together or orthogonal each other. The bipolar moments with $k_1 = 0$ appear in g_0 and those with $k_1 = 2$ appear in g_2. The moments with $K = Q = 0$ are isotropic in the space and thereby they do not accompany β in Eqs. 7 and 8.

C. Composite Doppler Profiles. As shown by Docker,[71] appropriate combinations of the Doppler profiles are composed to facilitate the analysis. The profiles measured in two or three LIF excitation-detection geometries for two different types of rotational transitions (P or R vs Q) give the composite Doppler profile, $D_0^K(k_1, k_2; v)$, which depends on a single bipolar moment $\overline{\beta_0^K(k_1, k_2; v')}$. A simple example for $j' = 0$ is shown in Fig. 2(b). In this case, the polarization of rotational angular momentum is absent and thus the two profiles are enough to obtain the composite profiles $D_0^0(0, 0; v)$ and $D_0^2(2, 0; v)$. Prior to taking linear combinations of the observed Doppler profiles, each profile is normalized according to the value of the rotational alignment $A_0^{(2)}$ (Ref. 31) of the probed rotational level:

$$A_0^{(2)} = \frac{2}{5}\beta\left\langle\overline{\beta_0^2(0, 2; v')}\right\rangle, \tag{9}$$

where $\langle ... \rangle$ represents the average over the product speed v'. Since the integral of $P_2(x)$ over $x = -1$ to 1 equals zero, as recognized from Eqs. 6 and 7, the integrated area of the line profile is proportional to $b_0 + 5b_1A_0^{(2)}/4$. Thus, $A_0^{(2)}$ is obtained from the two integrated line intensities measured at different polarization of the photolysis laser [geometries $\mathrm{I_a}$ and II in Fig. 6(b)]. Once $A_0^{(2)}$ is determined, the absolute intensity of each Doppler profile is not necessary for the Doppler shape analysis.

The details of the combinations to yield the adequate composite Doppler profiles are listed in Table 1. For example, the composite Doppler profile of (I + II + III)/3 for single rota-

Table 1. Combination and Weights of the Observed Doppler Profiles to Construct Composite Doppler Profiles

Geometry*	Intermediate composite Doppler profile	Weight factor**		Final composite Doppler profile***
		Q branch	P or R branch	
$\frac{1}{3}$(I + II + III)	$q_0D_0^0(0, 0; v) - q_2D_0^0(2, 2; v)$	$-q_2^{\mathrm{PR}}$	q_2^{Q}	$fD_0^0(0, 0; v)$
		$-q_0^{\mathrm{PR}}$	q_0^{Q}	$fD_0^0(2, 2; v)$
III − I	$3q_0D_0^2(2, 0; v) - \frac{6}{5}q_2D_0^2(0, 2; v)$	$-q_2^{\mathrm{PR}}$	q_2^{Q}	$3fD_0^2(2, 0; v)$
		$-q_0^{\mathrm{PR}}$	q_0^{Q}	$6fD_0^2(0, 2; v)/5$
III − II	$3q_0D_0^2(2, 0; v) + \frac{12}{7}q_2D_0^2(2, 2; v)$	$-q_2^{\mathrm{PR}}$	q_2^{Q}	$3fD_0^2(2, 0; v)$
		$-q_0^{\mathrm{PR}}$	q_0^{Q}	$-12fD_0^2(2, 2; v)/7$

*Geometries I, II, and III are those depicted in Fig. 6(b). **The intermediate composite Doppler profile of Q branch is multiplied by q^{PR}, which appears in that of P or R branch, and vice versa. The high-j limit values of q's in 1 + 1 LIF of Σ–Π transition are $q_0{}^{\mathrm{PR}} = 21/20$, $q_0{}^{\mathrm{Q}} = 9/10$, $q_2{}^{\mathrm{PR}} = -33/56$, and $q_2{}^{\mathrm{Q}} = 45/56$.[71] ***The coefficient, $f = q_2{}^{\mathrm{Q}}\, q_0{}^{\mathrm{PR}} - q_2{}^{\mathrm{PR}}\, q_0{}^{\mathrm{Q}}$ ($f \approx 1.4$ for high-j limit of Σ–Π transition).

tional line is proportional to $q_0D_0^0(0,\ 0;\ \nu)-q_2D_0^0(2,\ 2;\ \nu)$, where the coefficients q_0 and q_2 are related to $k_2 = 0$ and $k_2 = 2$, respectively. The important thing is that the q_0 and q_2 are different between P (or R) branch and Q branch. Thus, as shown in Table 1, with the appropriate weight factors q_0 and q_2, the addition of the two (I + II + III)/3 profiles measured in P (or R) branch and Q branch cancels $D_0^0(0,\ 0;\ \nu)$ or $D_0^0(2,\ 2;\ \nu)$. Since the composite Doppler profile $D_0^K(k_1,\ k_2;\ \nu)$ depends on a single bipolar moment $\overline{\beta_0^K(k_1, k_2; v')}$, thus obtained composite profile is expressed as[83]

$$D_0^K(k_1, k_2; \nu) = \int_{v_p}^{\infty} \frac{a_K}{2(\nu_0 v'/c)} \overline{\beta_0^K(k_1, k_2; v')} P_{k_1}\left(\frac{v_\mathrm{p}}{v'}\right) f(v')v'^2 \mathrm{d}v', \tag{10}$$

where $a_K = 1$ for $K = 0$ while $a_K = \beta/2$ for $K = 2$. The physical meaning of $D_0^K(k_1,\ k_2;\ \nu)$ is the same as that of $\overline{\beta_0^K(k_1, k_2; v')}$. Thus, the composite Doppler profiles $D_0^0(0,\ 0;\ \nu)$ and $D_0^2(2,\ 0;\ \nu)$ corresponding to the leading terms in g_0 and g_2 are related to the LAB speed distribution (population) and $\boldsymbol{\mu}$–$\mathbf{v}'$ correlation (anisotropy), respectively. Here, $\boldsymbol{\mu}$ is the transition dipole vector in the first photolysis process at $t = 0$. The other three composite Doppler profiles reflect the polarization of the product rotational angular momentum vector, $\mathbf{j}'$: $D_0^2(0,\ 2;\ \nu)$ for $\boldsymbol{\mu}$–$\mathbf{j}'$, $D_0^0(2,\ 2;\ \nu)$ for $\mathbf{v}'$–$\mathbf{j}'$, and $D_0^2(2,\ 2;\ \nu)$ for $\boldsymbol{\mu}$–$\mathbf{v}'$–$\mathbf{j}'$ correlations.

D. Polarization-Dependent Differential Cross Sections and the Angular Distribution in the CM Frame. The correlated angular distribution function in the CM frame, $P(\omega_\mathrm{t},\ \omega_\mathrm{r})$, is expressed as the expansion in the modified spherical harmonics $C_{kq}(\theta_\mathrm{r},\ \phi_\mathrm{r})$:

$$P(\omega_\mathrm{t}, \omega_\mathrm{r}) = \sum_{k,q} \frac{2k + 1}{4\pi} \frac{1}{\sigma} \frac{\mathrm{d}\sigma_{kq}}{\mathrm{d}\omega_\mathrm{t}} C_{kq}{}^*(\theta_\mathrm{r}, \phi_\mathrm{r}). \tag{11}$$

The coefficient in Eq. 11, $(1/\sigma)\ \mathrm{d}\sigma_{kq}/\mathrm{d}\omega_\mathrm{t}$, is polarization-dependent differential cross section (PDDCS),[78,83] where σ is the integral cross section of the state-to-state reaction and normalizes the PDDCSs. The PDDCS is the angular momentum polarization expressed by the spherical tensor of rank k and component q differentiated by scattering angle ω_t. For example, $\mathrm{d}\sigma_{00}/\mathrm{d}\omega_\mathrm{t}$ represents the ordinal differential cross section ($\mathbf{k}$–$\mathbf{k}'$ correlation) and $\mathrm{d}\sigma_{2q}/\mathrm{d}\omega_\mathrm{t}$ represents the anisotropic component of $\mathbf{j}'$ with respect to ω_t.

Aoiz et al. have shown the relationship between the bipolar moments $\overline{\beta_0^K(k_1, k_2; v')}$ in the v_1 frame and the PDDCSs in the CM frame.[83] As easily recognized, $\mathrm{d}\sigma_{00}/\mathrm{d}\omega_\mathrm{t}$ appears in $\overline{\beta_0^2(2, 0; v')}$ while $\mathrm{d}\sigma_{2q}/\mathrm{d}\omega_\mathrm{t}$'s appear in all the polarization-dependent moments, $\overline{\beta_0^2(0, 2; v')}$, $\overline{\beta_0^0(2, 2; v')}$, and $\overline{\beta_0^2(2, 2; v')}$. As described in the next subsection, based on this relationship, $\mathrm{d}\sigma_{kq}/\mathrm{d}\omega_\mathrm{t}$'s are determined by fitting all the $D_0^K(k_1,\ k;\ \nu)$ profiles simultaneously.

The angular distribution function $P(\omega_\mathrm{t},\ \omega_\mathrm{r})$ contains the complete information of the correlated angular distribution. However, the resolution of the present Doppler experiments is not so high as to discuss the angular distribution of $\mathbf{j}'$ dependent on the scattering angle. Thus, in the present review, the average angular distribution function $P(\theta_\mathrm{r},\ \phi_\mathrm{r})$, which is obtained by integrating $P(\omega_\mathrm{t},\ \omega_\mathrm{r})$ over the scattering angle ω_t, is used to discuss the stereodynamics of bimolecular reactions:

$$\begin{aligned} P(\theta_\mathrm{r}, \phi_\mathrm{r}) &= \int P(\omega_\mathrm{t}, \omega_\mathrm{r})\, \mathrm{d}\omega_\mathrm{t} \\ &= \sum_{k,q} \frac{2k + 1}{4\pi} a_{kq} C_{kq}{}^*(\theta_\mathrm{r}, \phi_\mathrm{r}), \end{aligned} \tag{12}$$

where

$$a_{kq} = \int \frac{1}{\sigma} \frac{\mathrm{d}\sigma_{kq}}{\mathrm{d}\omega_\mathrm{t}} \mathrm{d}\omega_\mathrm{t}. \tag{13}$$

As shown in Fig. 7, the azimuthal angle ϕ_r represents the angle between $\mathbf{j}'$ and the $\mathbf{k}$–$\mathbf{k}'$ plane since the $\mathbf{k}$–$\mathbf{k}'$ plane coincides with the xz plane by putting $\phi_\mathrm{t} = 0$.[83] Thus, the $P(\theta_\mathrm{r},\ \phi_\mathrm{r})$ expresses the scattering angle average of $\mathbf{j}'$ distribution with reference to the $\mathbf{k}$ vector and the $\mathbf{k}$–$\mathbf{k}'$ plane. Furthermore, the integration of the $P(\theta_\mathrm{r},\ \phi_\mathrm{r})$ over the appropriate azimuthal angle yields the angular distribution function $P(\cos\ \theta_\mathrm{r})$ and $P(\cos\ \theta_\mathrm{tr})$ representing the $\mathbf{k}$–$\mathbf{j}'$ and $\mathbf{k}'$–$\mathbf{j}'$ correlation, respectively, where θ_tr is the angle between $\mathbf{k}'$ and $\mathbf{j}'$. These angular distribution functions are also utilized to discuss the reaction dynamics.

E. The Fitting Procedure. The set of PDDCSs is determined from the least-squares fitting. The experimental composite Doppler profiles $D_0^K(k_1,\ k;\ \nu)$ are fit with the linear combination of the basis functions $B_0^K(k_1,\ k;\ \nu; f_\mathrm{T},\ \cos\ \theta_\mathrm{t};\ q)$:

$$D_0^K(k_1, k; \nu) = \sum_{f_\mathrm{T}} \sum_{\cos\theta_\mathrm{t}} \sum_{q} c_{kq}(f_\mathrm{T}, \cos\theta_\mathrm{t}) B_0^K(k_1, k; \nu; f_\mathrm{T}, \cos\theta_\mathrm{t}; q). \tag{14}$$

The basis functions $B_0^K(k_1,\ k;\ \nu; f_\mathrm{T},\ \cos\ \theta_\mathrm{t};\ q)$ represent the contribution of the rank k and component q of the PDDCSs, $(1/\sigma)\ \mathrm{d}\sigma_{kq}/\mathrm{d}\omega_\mathrm{t}$, to $D_0^K(k_1,\ k;\ \nu)$. The basis functions are resolved into a specific CM scattering angle θ_t and the fraction of the available energy (excluding the internal energy of the observed product) released into the product CM translational energy, f_T. For the PDDCSs independent of the rotational angular momentum polarization $(k = 0)$, f_T distribution and scattering angle distribution $\mathrm{d}\sigma_{00}/\mathrm{d}\omega_\mathrm{t}$ are determined by simultaneously fitting $D_0^0(0,\ 0;\ \nu)$ and $D_0^2(2,\ 0;\ \nu)$. For those dependent on the rotational angular momentum polarization $(k = 2)$, $\mathrm{d}\sigma_{2q}/\mathrm{d}\omega_\mathrm{t}$'s are determined by simultaneously fitting $D_0^2(0,\ 2;\ \nu)$, $D_0^0(2,\ 2;\ \nu)$, and $D_0^2(2,\ 2;\ \nu)$.

Figure 8 demonstrates an example of the basis functions for $k = 0$, $B_0^0(0,\ 0;\ \nu)$ and $B_0^2(2,\ 0;\ \nu)$, corresponding to the speed distribution and spatial anisotropy, respectively. The examples are calculated for the OH($^2\Pi_{3/2}$, $v' = 2$, $j' = 5.5$) products of O(^{1}D) + H_2O reaction, which is presented in Sec. IV. B. The OH products are scattered into the sphere whose radius is $w_\mathrm{OH} \equiv |\mathbf{w}_\mathrm{OH}|$ and the sphere is divided into the rings with the equal interval in $\mathrm{d}(\cos\ \theta_\mathrm{t})$. These basis functions are obtained after the integration over the magnitude and orientation of $\mathbf{v}_\mathbf{O}$, $\mathbf{v}_\mathbf{RH}$, and $\mathbf{w}_\mathbf{OH}$, i.e., the angle between the velocity vectors of O(^{1}D) and H_2O, the speed distributions of O(^{1}D) photofragment and thermal H_2O, the azimuthal angle of CM recoil vector of OH around the relative velocity vector $\mathbf{k}$, and the CM recoil energy depending on the collision energy and f_T. In calculating $\mathbf{v}_\mathbf{O}$, the effect of thermal motion of precursor N_2O is taken into account. The basis functions in Fig. 8 are those for $f_\mathrm{T} = 0.9$ and similar basis functions are prepared for other f_T's. As can be recognized from Fig. 8, the shapes of the basis functions change with the scattering angle. It is therefore possible to determine the product speed distribution and scattering angle dis-

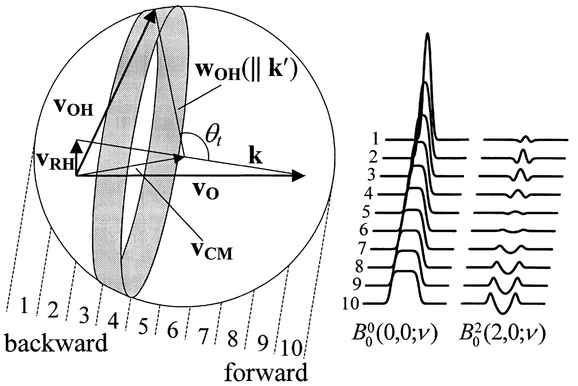

Fig. 8. The example of the basis functions to determine f_T distribution and scattering angle distribution. These distributions are obtained by simultaneously fitting $D_0^0(0, 0; v)$ and $D_0^2(2, 0; v)$ with the basis functions $B_0^0(0, 0; v)$ and $B_0^2(2, 0; v)$, respectively. The former corresponds to the speed distribution and the latter corresponds to the anisotropy of the products. The basis functions are calculated for the finite area of scattering sphere divided into the 3D rings with the equal interval in d(cos θ_t). The figures numbered for the basis functions correspond to that numbered for the rings. The shaded area represents the ring of No. 4. The examples are calculated for the OH($^2\Pi_{3/2}$, $v' = 2, j' = 5.5$) products of O(^{1}D) + H_2O reaction with $f_T = 0.9$. These basis functions are obtained after the integration over the magnitude and orientation of $\mathbf{v}_O$, $\mathbf{v}_{RH}$, and $\mathbf{w}_{OH}$. Note that the shapes of the basis functions change with the scattering angle even with such integration.

tribution, even with the considerable averaging in this bulb experiment. As for the basis functions for the speed distribution, $B_0^0(0, 0; v)$, the forward scattered products (cos $\theta_t > 0$) are faster and detected as a fat Doppler profiles, while the backward scattered products are slower and detected as a thin profiles. The anisotropy components, $B_0^2(2, 0; v)$, of forward scattered products are positive for large Doppler shifts and negative for small Doppler shifts. This type of shape is obtained when the Doppler profiles measured at geometry III ($\boldsymbol{\varepsilon}_p \parallel \mathbf{k}_a$) is wider than that measured at geometries I and II ($\boldsymbol{\varepsilon}_p \perp \mathbf{k}_a$) [see Fig. 6(b) and Table 1]. The $B_0^2(2, 0; v)$ of the most forward scattering is close to that of O(^{1}D) atoms since forward scattered products fly along the initial O(^{1}D) atom velocity, $\mathbf{v}_O$, in the LAB frame. The anisotropies of sideways scattered products (cos $\theta_t \approx 0$) are nearly zero since such directions make the magic angle of $P_2(\cos \Theta_{O\text{-}OH})$, where $\Theta_{O\text{-}OH}$ is the angle between $\mathbf{v}_O$ and $\mathbf{v}_{OH}$. This means the difference in geometries I, II, and III is small. By contrast, the backward scattered products (cos $\theta_t < 0$) fly perpendicular to $\mathbf{v}_O$ and thus their anisotropies have opposite sign against that of forward components. In this case, Doppler profiles are wider in geometries I and II than in geometry III. The set of coefficients $c_{kq}(f_T, \cos \theta_t)$ determined by the fitting procedure represents the set of f_T-resolved scattering angle dependences of PDDCSs. In this study, the f_T-integrated PDDCSs are mostly used to discuss the reaction dynamics. The integration of f_T-resolved DCS over cos θ_t gives a f_T distribution, which correlates with the internal energy distribution of the sibling products. The f_T region ranging from 0.0 to 1.0 was divided into several bins, while the region of cos θ_t ranging from -1.0 to 1.0 was divided into 10 bins. Several tens of basis functions were thereby used for the least-squares fitting. We carefully confirmed that, within statistical uncertainties, the f_T-integrated DCSs did not depend on the number of the basis functions used for the analysis.

For the preparation of the basis functions, the knowledge of the recoil velocity distribution and translational anisotropy of O(^{1}D) and O(^{3}P) is required. For O(^{1}D) produced from the 193 nm photodissociation of N_2O,[139,140] the recoil velocity distribution of O(^{1}D) reported by Felder et al.[139] was used. The recoil energy of O(^{1}D) is centered at 68 kJ/mol with FWHM of 25 kJ/mol and the average translational anisotropy is 0.48.[139] As described in elsewhere,[102] the recoil speed dependence of β[141–143] was taken into account. For O(^{3}P) produced from the NO_2 photodissociation, the speed distributions of O(^{3}P) were derived from the internal state distributions of the NO products reported by Zacharias et al.,[144] by considering the energy conservation. The translational anisotropy parameter β of O(^{3}P) was evaluated by measuring the Doppler profiles of the sister fragment NO($v' = 0$–2) for several rovibrational levels. The rovibrational-level dependent β values were 0.64–0.86 for 308 nm and 0.30–0.52 for 351 nm photolysis.[120] We used the average value of the β in the analysis of O(^{3}P) reactions and this approximation is supported by the study of NO_2 photodissociation.[145] We carefully confirmed that the variation of average β within the observed range did not produce any qualitative difference in the DCS. The orbital alignment of O($^1D_2$) observed in the recent studies[141–143,146] were not taken into account since the orbital alignment in the LAB frame is expected to be blurred due to the substantial averaging in the CM frame under the bulb experiment condition in this study.

The fitting procedure with non-orthogonal basis functions as attempted in this study has one of the notorious problems giving an unphysical solution in numerical analysis. To avoid this problem, we used the singular value decomposition method,[147] which generates a set of orthogonal basis functions from a set of original non-orthogonal functions. Furthermore, a maximum-entropy method[147] was utilized for eliminating physically meaningless solutions such as negative values of $c_{00}(f_T, \cos \theta_t)$ representing the product f_T-resolved DCS. Most analyses were carried out with the assumption that the reaction probability and the set of PDDCSs did not depend significantly on the initial translational energy (i.e., the collision energy) of the reactants. The only exception was the O(^{3}P) and hydrocarbon reaction, where the excitation function reported in Ref. 148 was taken into account.

IV. Stereodynamics of O(^{1}D) and O(^{3}P) Reactions

A. O(^{1}D) + Hydrocarbons. Reactions of an excited oxygen atom, O(^{1}D), with hydrocarbons (RH) yielding OH radicals play important roles in combustion and atmospheric chemistry:

$$\mathrm{O}(^1\mathrm{D}) + \mathrm{RH} \rightarrow \mathrm{OH}(^2\Pi) + \mathrm{R}. \qquad (15)$$

For saturated hydrocarbons, the exothermicity of this product channel is ≈200 kJ/mol and the alcohol intermediate locates ≈500 kJ/mol below the reagents.[60] The reactions with saturated hydrocarbons have been well characterized by the studies on product identification,[149–151] product-state distributions,[152–157] and scattering angular distribution.[88–90,110,158,159] These studies suggest that the insertion of the O(^{1}D) atom into a C-H bond forming an alcohol intermediate is dominant. The OH products are rovibrationally more excited than the statistical expectation. However, rotationally cold OH products especially in $v' = 0$ populate more significantly in the larger hydrocarbon reactions. In the rotational surprisal analysis (see e.g., Refs. 1–3), this trend shows a bimodal feature where the low-j' levels are colder than the statistical distribution while the high-j' levels are hotter than the statistical one.[152,154] This bimodality has been considered to suggest the possibility of the participation of two different mechanisms, each yielding either low-j' or high-j' component. Luntz proposed that these two components correspond to the abstraction (low j') and insertion (high j').[152] By contrast, Park et al. proposed the non-direct insertion (low j') and direct insertion (high j') mechanisms.[154] Thus, the origin of two components has been an intriguing point of these reactions.

We have measured the Doppler profiles of the low-j' ($j' = 6.5$) and high-j' ($j' = 13.5$) levels of the OH($^2\Pi_{1/2}$, $v' = 0$) products to compare the DCS.[101,105] The $j' = 6.5$ and $j' = 13.5$ levels correspond to the major levels in the population of the low-j' and high-j' components, respectively, in the surprisal analysis.[154] If the mechanisms between the two components are so different, the difference is possible to manifest in the DCS. The observed composite Doppler profiles, $D_0^0(0,\,0;\,v)$ and $D_0^2(2,\,0;\,v)$ of the $j' = 13.5$ level of C_2H_6 reaction[101]

$$\mathrm{O}(^1\mathrm{D}) + \mathrm{C_2H_6} \rightarrow \mathrm{OH}(^2\Pi) + \mathrm{C_2H_5} \qquad \Delta H^\circ(0) = -195\ \mathrm{kJ/mol} \quad (16)$$

is shown in Fig. 9. In this reaction, the population of $j' = 6.5$ level is slightly higher than that of $j' = 13.5$ level. The smooth solid lines in Fig. 9 represent the best fits and Fig. 10 shows thus determined f_T-integrated DCSs. Here, θ_t is the angle between $\mathbf{k}$ and $\mathbf{k}'$, i.e., the CM scattering angle (see Fig. 7). Figure 10 indicates that the DCSs for the OH($j' = 6.5$) and OH ($j' = 13.5$) are very close and have substantial intensities over the whole angular range, with slight preferences for backward scattering ($\cos\theta_t < 0$). As briefly reviewed above, the bimodal features in the rotational surprisal analysis for the saturated hydrocarbon reactions are more evident for the large hydrocarbon reactants.[152,154] For C_3H_8 reaction,

$$\mathrm{O}(^1\mathrm{D}) + \mathrm{C_3H_8} \rightarrow \mathrm{OH}(^2\Pi) + \mathrm{C_3H_7} \qquad \Delta H^\circ(0) = -193\ \mathrm{kJ/mol}, \quad (17)$$

the surprisal analysis shows that about 80% of $j' = 6.5$ products are regarded as the *cool* low-j' component.[152,154] In this reaction, the population of $j' = 6.5$ level is almost twice that of $j' = 13.5$ level. The observed DCSs of the OH($^2\Pi_{1/2}$, $v' = 0$) products in $j' = 6.5$ and $j' = 13.5$ levels of C_3H_8 reaction[105] are also similar and nearly isotropic as observed in the C_2H_6 reaction. Based on the traditional interpretation on a nearly isotropic DCS as observed here, the lifetimes of the intermediate complexes are comparable to or longer than at least a half rotational period; the estimated rotational period ranges from a few hundred femtoseconds to a few picoseconds, depending on the impact parameters. The observed DCSs suggest that both the *cool* low-j' and *hot* high-j' components originate in the insertion mechanism. Thus, the participation of the rebound abstraction mechanism giving backward scattered products in the

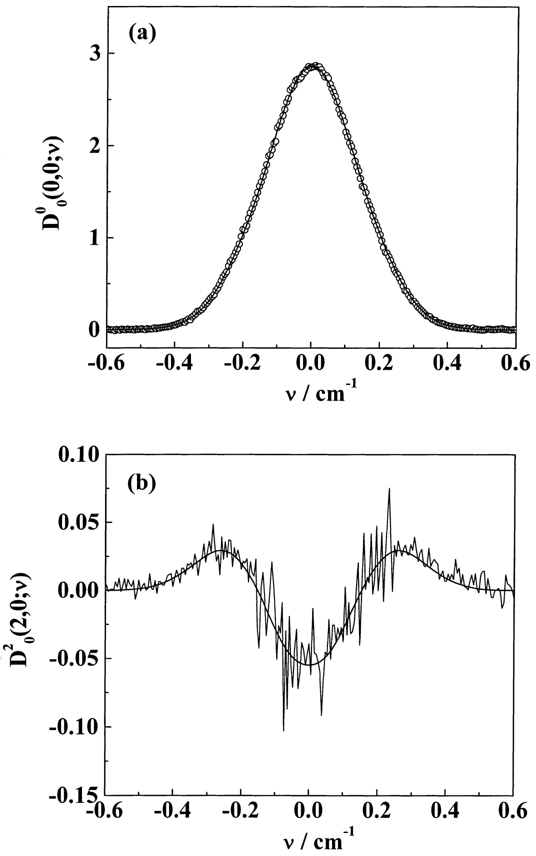

Fig. 9. The composite Doppler profiles for the product OH($^2\Pi_{1/2}$, $v' = 0$, $j' = 13.5$) generated from the reactions of O(^{1}D) with C_2H_6: (a) $D_0^0(0,\,0;\,v)$ (○) and (b) $D_0^2(2,\,0;\,v)$. Smooth solid lines are the best fits used for extraction of the product DCS and f_T distribution.

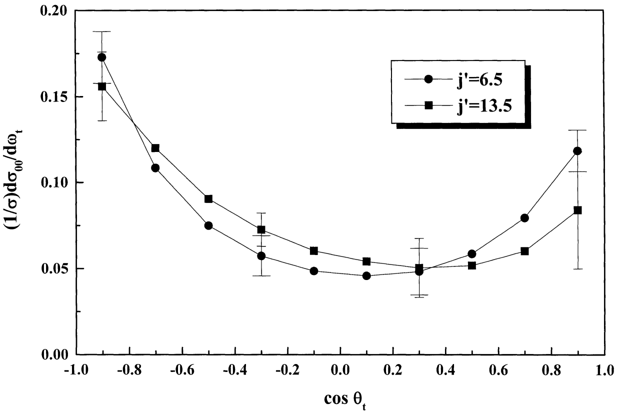

Fig. 10. The DCSs averaged over the recoil energy of the OH($^2\Pi_{1/2}$, $v' = 0$, j') products for the reactions of O(^{1}D) with C_2H_6: $j' = 6.5$ (●) and $j' = 13.5$ (■). Error bars correspond to $\pm 1\sigma$.

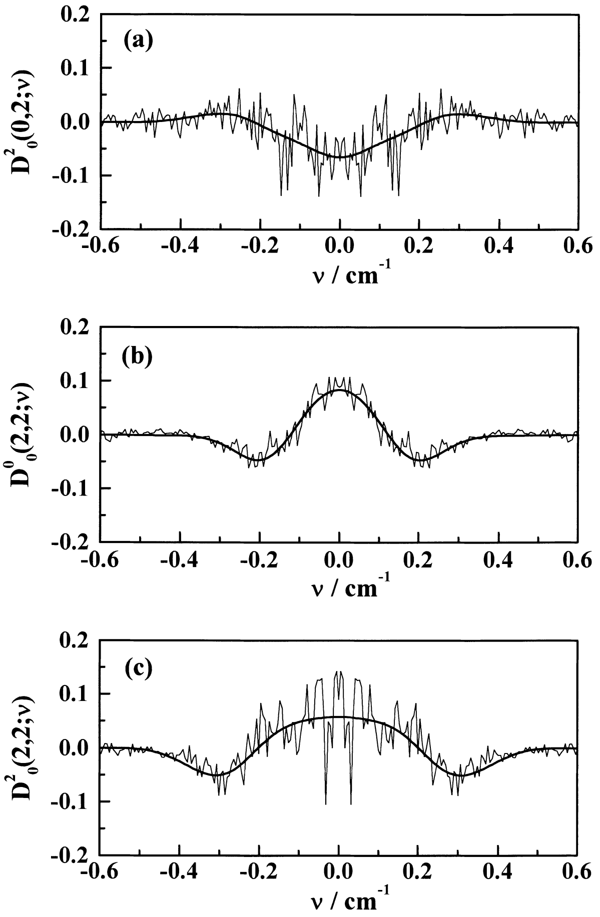

Fig. 11. The composite Doppler profiles for the product OH($^2\Pi_{1/2}$, $v' = 0, j' = 13.5$) generated from the reaction of O(^{1}D) with C_2H_6: (a) $D^2_0(0, 2; \nu)$, (b) $D^0_0(2, 2; \nu)$, and (c) $D^2_0(2, 2; \nu)$. Smooth solid lines are the best fits in the analysis of the rotational angular momentum polarization.

low-j' component proposed by Luntz[152] is not likely. On the other hand, if the direct and non-direct insertion mechanism proposed by Park et al.[154] is true and the direct insertion is prompt enough, an anisotropic DCS could be expected for high j'. However, the observation shows that the two types of the insertion mechanisms, even if operative, do not differ in DCS. This suggests that the difference in the mechanism between low-j' and high-j' components is not as simple as Park et al. proposed. Park et al. considered the non-direct insertion mechanism of low-j' component as statistical since this cool low-j' component decreases with OH(v') and its dependence on v' agreed with the vibrational distribution of OH obtained from a simple RRKM estimation.[154] However, the rotational distribution of low-j' component is too cool as compared with the statistical distribution. Thus, the mechanism of this insertion reaction has not been established yet.

As for the rotational angular momentum polarization, Fig. 11 shows the set of observed composite Doppler profiles, $D^2_0(0, 2; \nu)$, $D^0_0(2, 2; \nu)$, and $D^2_0(2, 2; \nu)$ of the product OH($j' = 13.5$) in the C_2H_6 reactions. The smooth solid lines in Fig. 11 represent the best fits in the analysis of the rotational angular momentum polarization. Figure 12(a) shows thus obtained angular distribution functions $P(\theta_r, \phi_r)$ representing the angular correlation among **k**, **k′** and **j′** derived by using Eq. 12. Here, θ_r is the polar angle between **k** and **j′**, and ϕ_r is the dihedral angle between the **k**–**k′** plane and **k**–**j′** plane (see Fig. 7). In Fig. 12(a), $P(\theta_r, \phi_r)$ shows two distinct peaks near $(\theta_r, \phi_r) = (90°, 90°)$ and (90°, 270°). These peaks correspond to the angular correlation where **j′** is simultaneously perpendicular to the **k** vector and the **k**–**k′** plane. The OH($^2\Pi_{1/2}$, $v' = 0, j' = 13.5$) products of the CH_4 and C_3H_8 reactions similarly have peaks perpendicular to **k**–**k′** plane. The correlation of **j′** ⊥ **k**–**k′** plane means that the POR of the OH products coincides with the **k**–**k′** scattering plane. Since the incoming orbital angular momentum (≈ 50$\hbar$) is large compared with the rotational angular momentum of the hydrocarbons (≈ 10$\hbar$), this orbital motion determines the POR of a collision complex. Thus, the **j′** ⊥ **k**–**k′** correlation is produced when the C–O–H plane lies in this plane and the in-plane C–O–H bending motion generates the OH rotation. In this case, the **k**–**k′** scattering plane coincides with the POR of the collision complex and that of OH. It is highly probable that the H atom in the C–O–H moiety lies in this rotational plane since the deep potential well attracts the O(^{1}D) atom to the center of the C-H bond. Thus, it can be considered that the prominent peaks at $(\theta_r, \phi_r) = (90°, 90°)$ and (90°, 270°) support the insertion mechanism suggested by the isotropic DCS and the previous studies.[152,154–157] It should be

(a) C2H6

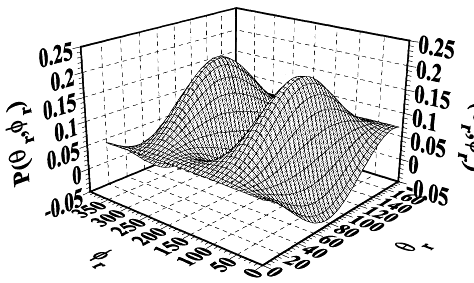

(b) C2H4

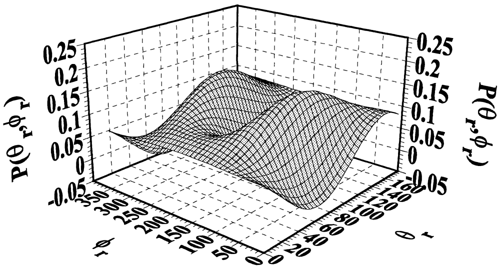

Fig. 12. Angular distribution functions representing polarization of the rotational angular momentum vector **j′** for the product OH($^2\Pi_{1/2}$, $v' = 0, j' = 13.5$) generated from the reactions of O(^{1}D) with C_2H_6 and C_2H_4: (a) the polar plots of $P(\theta_r, \phi_r)$ representing the angular correlation between **j′** and the collision plane for the reactions of O(^{1}D) with C_2H_6, (b) the polar plots of $P(\theta_r, \phi_r)$ for the reaction of C_2H_4.

noted that the insertion mechanism does not mean the complete randomization within a complex. As observed here, the origin of OH rotation is strongly correlated to C–O–H bending motions. In contrast to the $j' = 13.5$ products, the rotational angular momentum polarization of $j' = 6.5$ products is not strong and depends on the Λ doublets. It suggests that the in-plane torque participates to generate low j' products and the nonadiabatic exit channel interaction depending on the Λ-doublet levels is operative. However, the high j' levels are dominant in these reactions[152,154] and thus the contribution of the C–O–H bending motion is considered to be significant for these reactions.

In the above discussion, one should be careful whether the high and broad collision energies ($\langle E_{\rm col} \rangle \approx 50$ kJ/mol and FWHM ≈ 35 kJ/mol) of our experimental condition affect the reaction mechanism severely or not. We have confirmed that the bimodal features in the rotational distributions are observed in our high collision energy conditions. The detailed analysis of the PDDCSs shows that the $f_{\rm T}$ distribution and rotational angular momentum polarization are very similar in the backward and forward scattering components. Thus, it is not highly plausible that the observed isotropic angular distribution is comprised of backward-scattered abstraction and forward-scattered stripping both in the peripheral region, since these two mechanisms do not necessarily behave in the same way. Another problem associated with the high collision energies are the participation of the excited state surfaces. It has been turned out that the contribution of the excited state surface becomes significant for the collision energies larger than 10 kJ/mol in $O(^1D) + H_2$ reaction.[50–52] The excited state surfaces originate in the five-fold degeneracy of $O(^1D_2)$ atom and thus the contribution of the excited states will be general for $O(^1D)$ atom reactions. The $O(^1D) + H_2$ reaction have some similarities to the $O(^1D) + RH$ reactions for the feature of the ground state PES and the product OH state distribution. In the $O(^1D) + H_2$ reaction, the excited states yield the vibrationally highly excited and rotationally very cold OH products since the excited surfaces have collinear saddle point and the main pathway is the abstraction of H atom with strong backward scattering. If the dynamics of the excited states are also similar between the $O(^1D) + H_2$ and $O(^1D) + RH$ reactions, the effects mostly manifest in the products in the high v' and low j' levels. Thus, the observed correlation of $\mathbf{j}' \perp \mathbf{k}$–$\mathbf{k}'$ for the OH($v' = 0, j' = 13.5$) can be considered to represent the dynamics on the ground state PES.

A recent quasi-classical trajectory (QCT) study on the $O(^1D) + CH_4$ reaction with an ab initio PES showed that the reaction takes place almost exclusively through the insertion pathways.[160,162] In this QCT study, the lifetimes of the collision complexes are estimated from the time evolution of the trajectories though the calculation was performed under the O–H–(CH$_3$) triatomic approximation, where the calculated lifetime cannot be considered strictly accurate. The lifetimes range from 0.04 to 2.00 ps and the average value is 0.20 ps. The average rotational period of the intermediate complex of this reaction is estimated to be a few hundred fs from the average collision condition used in this study. Compared with this average rotational period, some of the trajectories in the QCT calculation spend a very short time as the intermediate complexes. It should be noted that these short-lived trajectories do not correspond to direct stripping or abstraction in the peripheral region, since these trajectories also exhibit the formation of the C–O–H bond.[160,161] Therefore, these short-lived insertion trajectories also contribute to the observed nearly isotropic DCSs. A plausible explanation is as follows. The short-lived collisions with large impact parameters are scattered forward and those with small impact parameters are scattered backward as in the hard-sphere elastic collision. Irrespective of the impact parameters, these reactive collisions pass once through the C–O–H configuration of alcohol-type potential well. Even though the lifetime is short, the transient C–O–H configuration generates the in-plane bending torque and thus the rotational angular momentum polarization of $\mathbf{j}' \perp \mathbf{k}$–$\mathbf{k}'$ plane is commonly observed, irrespective of the scattering angle. In this picture, the lifetimes of such short-lived insertion of forward-scattering trajectories correspond to the time required to pass the C–O–H region. By contrast, the backward-scattering trajectories of short-lived insertion will exhibit the prompt flip from the collinear $O(^1D)$–H–CH$_3$ geometry to the HO–CH$_3$ geometry. As a support of this picture, an ab initio calculation of $O(^1D)$–CH$_4$ surface suggested the strong possibility of off-axis O atom migration to form the stable CH$_3$OH structure after passing a very low potential barrier in the collinear $O(^1D)$–H–CH$_3$ approach.[163]

Compared with saturated hydrocarbon reactions, less attention has been paid to the reactions with unsaturated hydrocarbons. The insertion pathway was suggested as the dominant mechanism from a product analysis observing stabilized keto-type species in $O(^1D)$ reaction with C_3H_6 (Ref. 164) and a rovibrational state measurement for $O(^1D)$ and C_2H_4 reaction.[165] The reaction of $O(^1D)$ with the smallest unsaturated hydrocarbon, C_2H_4,

$$O(^1D) + C_2H_4 \rightarrow OH(^2\Pi) + C_2H_3 \qquad \Delta H^\circ(0) = -166 \text{ kJ/mol} \quad (18)$$

has been exploited by the measurement of OH internal state distributions.[165] The rovibrational state distributions and a preferential population of the $\Pi(A')$ Λ-doublet component are also quite similar to that observed in the reaction of C_2H_6.[152,154,156,157] This similarity between the C_2H_4 and C_2H_6 reaction suggests that a similar mechanism is dominant in both reactions. We have performed the Doppler analysis for the $O(^1D) + C_2H_4$ reaction for OH($^2\Pi_{1/2}$, $v' = 0$, $j' = 6.5$, 13.5) products. The DCSs of the OH($j' = 6.5$) and OH($j' = 13.5$) in the C_2H_4 reaction are very similar to those in the C_2H_6 reaction shown in Fig. 10. More interesting is the angular distribution of $\mathbf{j}'$, $P(\theta_r, \phi_r)$, plotted in Fig. 12(b). For C_2H_4 reaction, although the global feature of the $P(\theta_r, \phi_r)$ is similar to that of the C_2H_6 reaction, the peaks at $(\theta_r, \phi_r) = (90°, 90°)$ and $(90°, 270°)$ are weaker than those in C_2H_6 reaction. To clarify the origin for this difference, the $\mathbf{k}'$–$\mathbf{j}'$ angular distributions, namely, $P(\cos \theta_{\rm tr})$, are plotted for both the reactions in Fig. 13. The $\mathbf{k}'$–$\mathbf{j}'$ correlations of both reactions are quite similar and clearly peaked at $\cos \theta_{\rm tr} = 0$, i.e., $\mathbf{j}' \perp \mathbf{k}'$. Since the $\mathbf{k}'$–$\mathbf{j}'$ angular correlation is determined only in the exit channel, the C–O–H bending motion in the alcohol-type intermediate complex is considered to dominate the product rotation also in the C_2H_4

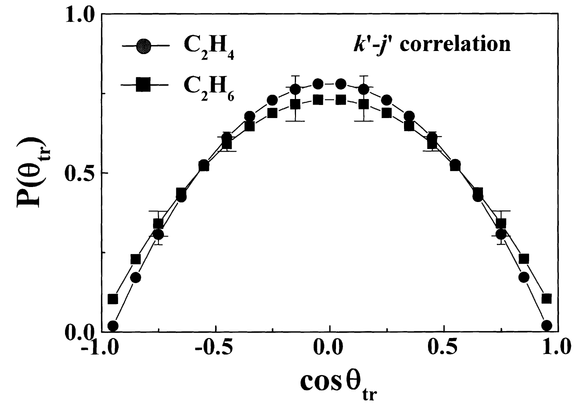

Fig. 13. The angular correlation between **j′** and the relative velocity vector of the products, **k′** of the O(^{1}D) with C_2H_4 and C_2H_6 reactions.

reaction. The common origin of the product rotation in both reactions is consistent with the similarity of the rotational distributions between these two reactions reported in the previous studies.[152,154,156,157,165] For the C_2H_4 reaction, the weak angular correlation between **j′** and **k–k′** plane together with the strong **k′–j′** correlation implies the weak **k–j′** correlation. The weak **k–j′** correlation in C_2H_4 reaction suggests the weak spatial relation between the incident velocity vector of the oxygen atom (**k**) and the C–O–H plane, which determines the plane of OH rotation. In the C_2H_4 reaction, the aspect of dynamics after the insertion different from the C_2H_6 reaction is the presence of the tautomerization process, where the direct 1,3-H atom shift from the O atom to the β-C atom in the vinyl alcohol complex yields acetaldehyde. In this process, a relatively large change of the C–C–O angle to let the migrating H atom come close to the β-C atom is necessary and such motions cause some movement of the C–O–H plane relative to the incident direction of the oxygen atom. Therefore, the weak **k–j′** correlation observed for the C_2H_4 reaction indicates that the OH formation occurs during the tautomerization from vinyl alcohol to acetaldehyde. As another pathway in ethylene reaction, the ethylene oxide produced by O(^{1}D) insertion into C=C bond may be a possible intermediate. The ethylene oxide was suggested to locate ≈800 kJ/mol below the reactants.[166] In spite of such large stability, this type of adduct was not observed in the high-pressure product analysis for O(^{1}D) reaction with C_3H_6.[164] The possibility of the formation of this adduct can not be ruled out if the OH products were finally produced from the alcohol intermediate. However, the adduct formation is not expected to be highly plausible for H atom abstraction from this adduct since the dynamical constraint of this pathway is considered to be weak to yield the **k′–j′** correlation as strong as the O(^{1}D) + C_2H_6 reactions.

B. O(^{1}D) + H$_2$O. The reaction of O(^{1}D) with H_2O has a large rate constant (2.2×10^{-10} cm^3 molecule^{-1} s^{-1})[60] and produces two OH radicals:

$$\mathrm{O(^1D)} + \mathrm{H_2O} \rightarrow \mathrm{OH(^2\Pi)} + \mathrm{OH(^2\Pi)} \qquad \Delta H^\circ(0) = -120\ \mathrm{kJ/mol} \quad (19)$$

This reaction is the major source of OH radicals in the stratosphere. The possible intermediate of this reaction is HOOH, which locates 328 kJ/mol below the reactant species. The two OH product molecules produced from this reaction are chemically identical, but their origins are distinctly different, i.e., "new" OH formed in the reaction and "old" OH present in the H_2O reagent from the beginning. This reaction has been studied with isotopically labeled $H_2{}^{18}O$ reagents to distinguish the two types of OH products.[113,167–176] From the product-state distribution measurements, it has been found that the newly formed ^{16}OH is vibrationally and rotationally much more excited than the old ^{18}OH. However, as seen in the hydrocarbon reactions, it is also intriguing to determine whether this reaction proceeds via the direct abstraction, stripping or insertion pathway. The asymmetric energy partitioning between the chemically identical product species has invoked an idea of the direct mechanism[113,167–170,172–176] such as abstraction or stripping. This idea is based on the traditional concept; the insertion mechanism causes the energy randomization within the stable complex and does not yield the asymmetric energy partitioning. As opposed to such speculation, Cleveland et al. proposed a short-lived insertion mechanism.[171]

In addition to the product-state distribution measurements, King et al. attempted a Doppler study.[113] However, they only measured the linewidths of the Doppler profiles and did not analyze the Doppler line shapes. The full analysis of the Doppler profiles is therefore needed and we have reexamined this reaction for OH($^2\Pi_{3/2}$, $v' = 2, j' = 5.5$) products to selectively observe the newly formed OH.[102] This selection is possible for isotopically unlabeled normal H_2O reagents used in this study since the previous works reported that the amount of the old OH in $v' = 2$ was negligible.[171,172]

Figure 14 shows the composite Doppler profiles $D_0^0(0, 0; v)$ and $D_0^2(2, 0; v)$. The total DCS averaged over the whole f_T region is displayed in Fig. 15. The DCS has substantial intensities over a wide angular range, with slight preference for backward scattering. This result cannot be predicted either from the direct abstraction mechanism yielding backward-peaking DCS or from the direct stripping mechanism yielding forward-peaking DCS. Figure 16 shows the CM angular distribution function of **j′**, $P(\theta_r, \phi_r)$. The overall pattern of the $P(\theta_r, \phi_r)$ for O(^{1}D) + H_2O reaction is very similar to that observed for O(^{1}D)–hydrocarbon reactions [see Fig. 12(a)]. The two peaks near $(\theta_r, \phi_r) = (90°, 90°)$ and $(90°, 270°)$ again imply that **j′** is predominantly perpendicular to the **k–k′** plane. This preference is explained from the HOOH collisional complex formation and a primary contribution of the bending motion of the H–O–O moiety to the product rotation. A detailed analysis of PDDCSs shows that the product OH scattered both in the forward and backward hemispheres exhibit almost the same $P(\theta_r, \phi_r)$. This suggests that, irrespective of the scattering angle, the reaction is dominated by the same mechanism. Therefore, as discussed in the O(^{1}D)–hydrocarbon reactions, the nearly isotropic DCS most probably indicates that the reaction proceeds via an insertion pathway involving the formation of an intermediate HOOH complex which survives for a time comparable to its rotational period. As noticed for O(^{1}D)–hydrocarbon reactions, to discuss the reaction mechanism, one should be careful whether the high collision energy of the current condition affect the stereodynamics or not, since the OH($v' = 2, j' = 5.5$)

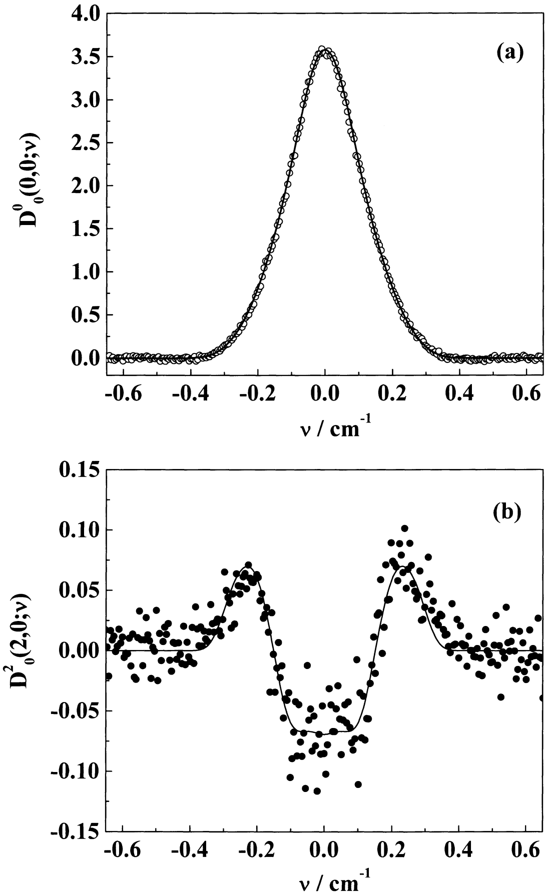

Fig. 14. The composite Doppler profiles for the product OH($^2\Pi_{3/2}$, $v' = 2, j' = 5.5$) generated from O(^{1}D) + H_2O reaction: (a) $D^0_0(0, 0; \nu)$ (○) and (b) $D^2_0(2, 0; \nu)$ (●). The smooth solid lines are the best fits in the Doppler analysis.

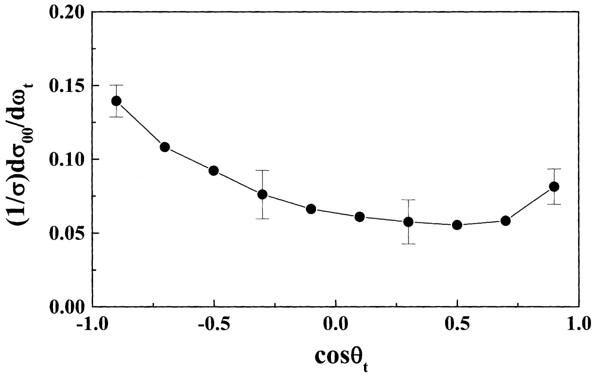

Fig. 15. The DCS averaged over the whole f_T region for the product OH($^2\Pi_{3/2}$, $v' = 2, j' = 5.5$) generated from O(^{1}D) + H_2O reaction. The error bars correspond to ±1σ.

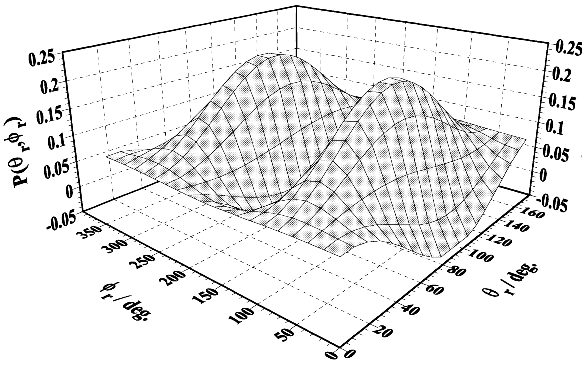

Fig. 16. Polar plots of $P(\theta_r, \phi_r)$ representing the angular distributions of the rotational angular momentum vector of the product OH($^2\Pi_{3/2}$, $v' = 2$, $j' = 5.5$) generated from O(^{1}D) + H_2O reaction.

product is in the highest vibrational channel and in a relatively low rotational level, where the contribution of exited surfaces is expected to be large. However, the contribution of excited state surfaces for this product channel is considered to be very little since the observed DCS and $P(\theta_r, \phi_r)$ differ those of rebound abstraction. Furthermore, the similar trend of the peak at **j′** ⊥ **k**–**k′** plane is observed for OH($v' = 0, j' = 19.5$) products. In this level, the new OH populates three times as the old one. Thus, the dominance of the bending motion as the origin of the OH rotation is not specific for OH($v' = 2, j' = 5.5$) products and it can be observed for both OH products. Sayós et al. have recently performed QCT calculation under the H–O–(OH) triatomic approximation and presented good agreement with our conclusion. The calculation shows that nearly all the reactive trajectories take place through the insertion mechanism and the **k**–**j′** and **k′**–**j′** correlations peak at 90°.[177] They have also calculated the minimum energy path (MEP) of this reaction.[178] In their ab initio MEP, the H_2O_2 intermediate is formed through a symmetric H_2O–O(^{1}D) minimum and breaks into OH products. Large H–O–O bending torque throughout this MEP is clearly consistent with our conclusion.

C. O(^{1}D) + N_2O. The reaction of O(^{1}D) with N_2O has a large rate constant ≈10^{-10} cm^3 molecule^{-1} s^{-1} (Ref. 60) and yields two NO product molecules:

$$\mathrm{O(^1D) + N_2O \rightarrow NO(^2\Pi) + NO(^2\Pi)} \qquad \Delta H^\circ(0) = -343\ \mathrm{kJ/mol} \quad (20)$$

This channel is one of the key reactions in atmospheric chemistry especially for the NO_x cycle of the ozone depletion. The branching ratio between this channel and the N_2 + O_2 channel was reported to be almost unity, with a slight dominance of the NO + NO channel.[60] The dynamics of this highly exothermic reaction has attracted much interest and has been extensively studied by measuring the product internal state distributions[179–185] and vector properties.[85–87] Although there were some discrepancies between the reported rovibrational distribution, substantial rovibrational excitation of the NO products has been observed. As seen in the O(^{1}D) + H_2O reaction, the two NO products of this reaction are generated from distinctly different origins: the "new" NO and "old" NO. Akagi et al. have recently determined the full vibrational distributions of NO($v' = 0$–17) and the relative ratio between the new and old NO products by using isotopically labeled reagents.[183,184] The results show that the old NO peaking at $v' = 0$ monotonically decreases with v' and the new NO peaking around $v' = 1$ is broadly distributed in the $v' < 10$ region. In high vibrational levels $v' > 10$, the new NO products populate more than the old ones. The difference in the vibrational distribution of the new NO and old NO is evident. However, the difference is not significant and the population of the new NO in the $v' > 10$ level is almost the same as that of the old NO in the $v' - 1$ level up to the energetic limit of the exothermicity. The rotational energy distribution of the NO($v' = 0$) is described with a Boltzmann distribution of $T_{rot} \approx 10000$ K. A comparison with a prior distribution shows that the rotational distribution of the nascent NO($v' = 0$) is close to the statistical distribution.[103,186] Furthermore, the rotational distributions of the two types of NO products were very similar.[187] All these results suggest that energy randomization between the two types of NO occurs to a considerable extent. For this reaction, spectroscopically observed *cis*-planer NO dimer[188,189] of near rectangular shape is a possible intermediate species and this ONNO minimum was shown to be on the MEP obtained by ab initio calculation.[190,191] However, the depth of the potential well of the NO dimer, 8.5 kJ/mol,[192] is considered too small to induce the observed energy randomization. Thus, the O(^{1}D) + N$_2$O reaction gives an outcome which is quite puzzling from the traditional considerations.

We have measured the state-resolved DCS and the rotational angular momentum polarization of the product NO($v' = 0$).[103] In the present study, although the two NO products are not isotopically distinguished, the observed NO($v' = 0$) products are considered mainly as the "old" NO since the population of the old NO in $v' = 0$ was found to be three times larger than that of the new NO.[184] Figure 17 shows the observed composite Doppler profiles $D_0^0(0, 0; \nu)$ and $D_0^2(2, 0; \nu)$ for the NO($^2\Pi_{1/2}$, $v' = 0, j' = 34.5$). Figure 18 presents the product CM translational energy distribution obtained from the DCS analysis for Fig. 17. The translational energy distribution is described as a Boltzmann distribution with $T_{trans} \approx 13000$ K and, though slightly colder, roughly close to a statistical prediction as observed for the rotational energy distribution. The wide spread of the translational energy distribution suggests that the sister products of the observed NO($v' = 0$) distribute over various rovibrational states.

The total DCS averaged over the recoil energy of the product NO($^2\Pi_{1/2}$, $v' = 0, j' = 34.5$) is shown in Fig. 19. The DCS shows substantial intensities over the whole angular range with a slight preference for backward scattering. A nearly isotropic product DCS is ordinarily attributed to the long lifetime of a collision complex comparable to or longer than its rotational period. If the intermediate of the reaction has a long lifetime, the observed nearly statistical energy distributions of the products can be consistently understood. However, since the O(^{1}D) + N$_2$O reaction is known to have no deep potential well, the lifetime of the complex is not expected to be quite long. For the present reaction, a QCT calculation on a London–Eyring–Polanyi–Sato (LEPS) surface was carried out and the result suggested that the lifetime of the collision complex was at most 1 ps, although the triatomic approximation was adopted for the calculations.[193] We estimated the rotational period of the possible intermediate of the *cis*-planer ONNO complex[190] to be about 1.8 ps by using the rotational constants of *cis*-NO dimer[194] and the average initial orbital angular momentum ($\approx 50\hbar$) of the reactants. The lifetime of the collisional ONNO complex corresponds to about half of its rotational period and cannot fully explain the nearly isotropic DCS obtained here.

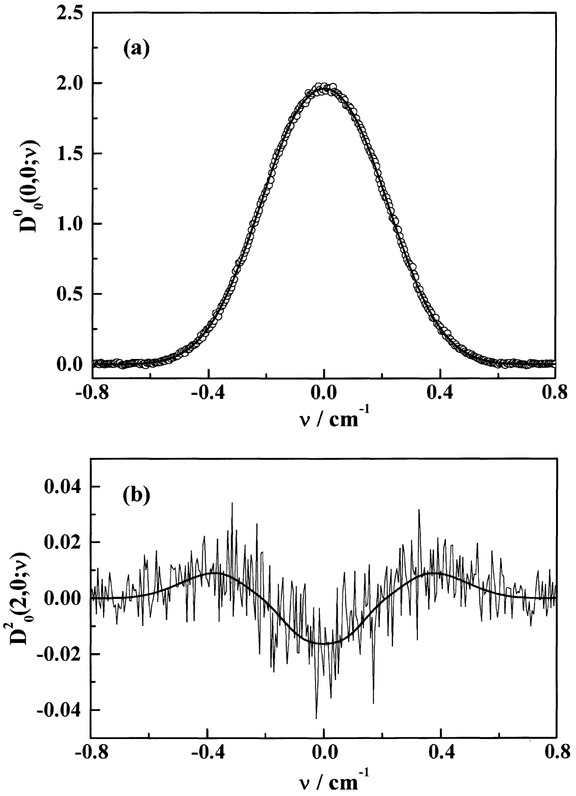

Fig. 17. Observed composite Doppler profiles for the product NO($^2\Pi_{1/2}$, $v' = 0, j' = 34.5$): (a) $D_0^0(0, 0; \nu)$ (○) and (b) $D_0^2(2, 0; \nu)$. Smooth solid lines in the two panels are best fits in the Doppler analysis extracting the product DCS and CM recoil energy distribution.

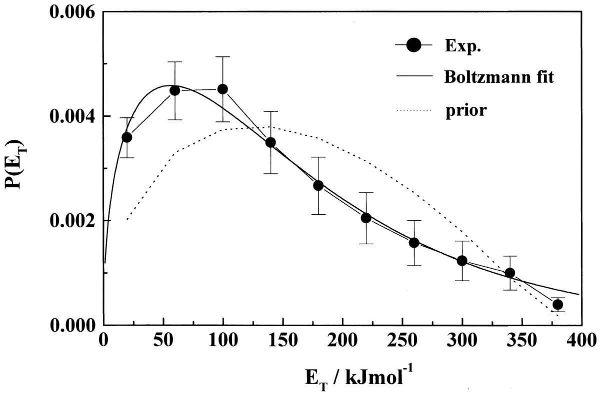

Fig. 18. The CM translational energy distribution given to the NO($^2\Pi_{1/2}$, $v' = 0, j' = 34.5$) and its sister fragment (●). Solid and dotted lines represent Boltzmann fit ($T_{trans} \approx$ 13000 K) and a prior distribution, respectively. Error bars correspond to $\pm 1\sigma$. The distribution is, though slightly colder, roughly close to a statistical prediction.

The spread of scattering angle for the reaction which does not involve a long-lived complex is usually related to the spread of the impact parameters. Since the total cross section of this reaction is very large, collisions with wide range of impact parameters can contribute to the reaction. Such wide spread of opacity function generally gives rise to the scattering of the

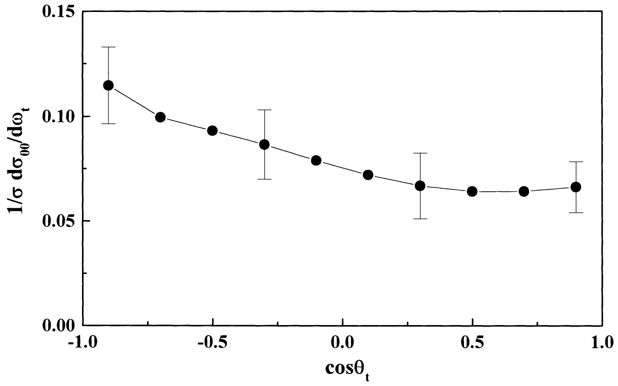

Fig. 19. The DCS for the NO($^2\Pi_{1/2}$, $v' = 0, j' = 34.5$) averaged over the recoil energy. Error bars correspond to $\pm 1\sigma$. The DCS shows substantial intensities over the whole angular range with a slight preference for backward scattering.

products over a wide angular range, as also suggested in the QCT calculation for the reaction O(^{3}P) + CS → CO + S.[96] We therefore attribute the nearly isotropic DCS to both the wide range of impact parameters and the lifetime of the collision complex, comparable to half of its rotational period.

Figure 20 shows the observed composite Doppler profiles $D^2_0(0, 2; \nu)$, $D^0_0(2, 2; \nu)$, and $D^2_0(2, 2; \nu)$, reflecting the polarization of rotational angular momentum vector $\mathbf{j}'$ of the NO($v' = 0, j' = 34.5$). The angular distribution function $P(\theta_r, \phi_r)$ derived from these composite Doppler profiles is shown in Fig. 21(a). Distinctly different from the reaction of O(^{1}D) with hydrocarbons or water, the $P(\theta_r, \phi_r)$ plot is almost flat. The isotropic $P(\theta_r, \phi_r)$ shows that there is no noticeable spatial angular correlation between $\mathbf{j}'$ and the $\mathbf{k}$–$\mathbf{k}'$ scattering plane. In order to examine this weak spatial correlation between $\mathbf{j}'$ and the collision plane in more detail, the distribution functions $P(\theta_r)$ and $P(\theta_{tr})$ representing the angular correlations of $\mathbf{k}$–$\mathbf{j}'$ and $\mathbf{k}'$–$\mathbf{j}'$, respectively, are shown in Figs. 21(b) and (c). These nearly flat distribution functions imply that $\mathbf{j}'$ is almost isotropic with respect to both $\mathbf{k}$ and $\mathbf{k}'$. If the in-plane bending motion of the N–N–O moiety contributes primarily to the product rotation, $\mathbf{j}'$ should have a preference for the angular correlation perpendicular to $\mathbf{k}'$. Therefore, the isotropic feature of $\mathbf{k}'$–$\mathbf{j}'$ correlation indicates that both the in-plane and out-of-plane motions contribute to the product rotation to almost the same degree.

As described above, we have found the nearly statistical rotational and translational distributions and participation of both the in-plane and out-of-plane motions of collision complex. Furthermore, the vibrational energy distributions of two types of NO products have been found to be closer to statistical prediction than that generally expected from a direct reaction process[182,184] and the rotational distributions of two types of NO products were suggested to be very similar.[187] These results can be consistently interpreted if there was a quite efficient energy redistribution in the complex within a very short period.

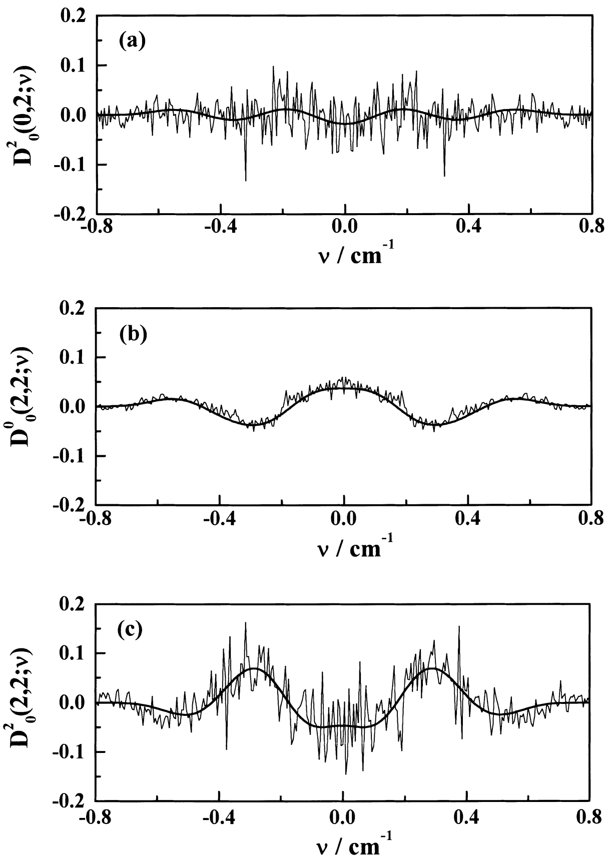

Fig. 20. Observed composite Doppler profiles for the product NO($^2\Pi_{1/2}$, $v' = 0, j' = 34.5$): (a) $D^2_0(0, 2; \nu)$, (b) $D^0_0(2, 2; \nu)$, and (c) $D^2_0(2, 2; \nu)$. The smooth solid lines are the best fits in the analysis extracting the product angular momentum polarization.

As discussed in the previous subsections, O(^{1}D) reactions with hydrocarbons or H_2O have shown nonstatistical behavior in the product-state distribution. The trend is consistent with the dominance of the in-plane bending motion in the torque generating the product rotation. Although these reactions have the deep potential well corresponding to the stable intermediate of alcohol or HOOH, the product-state distributions of these reactions are not necessarily statistical. In addition to these reactions, H(^{2}S) + CO_2 → OH + CO, is also well known to have the stable HOCO intermediate[195] and exhibits rotationally cold nonstatistical energy partitioning.[196] The recent Doppler study for this reaction performed by Brouard et al. have shown the dominant contribution of out-of-plane torque to the OH rotation.[95] This result is also consistent with the specific energy partitioning in this reaction. As opposed to these nonstatistical reactions with stable intermediates, the O(^{1}D) + N_2O reaction is rather statistical even without a deep potential well. Thus, different from the expectation traditionally written in the textbooks of chemical reaction dynamics,[1–4] the deep potential well does not seem essential for efficient energy redistribution. Although the ordinary argument connects the efficiency of energy randomization with the lifetime of the reactive intermediate, the most essential condition for the energy randomization is the strength of couplings among the internal modes of the intermediate.

To consider the efficient energy flow in the O(^{1}D) + N_2O, the difference between normal mode and local mode characters gives an invaluable hint. For the molecules containing two equivalent bonds with a common vibrational frequency, the en-

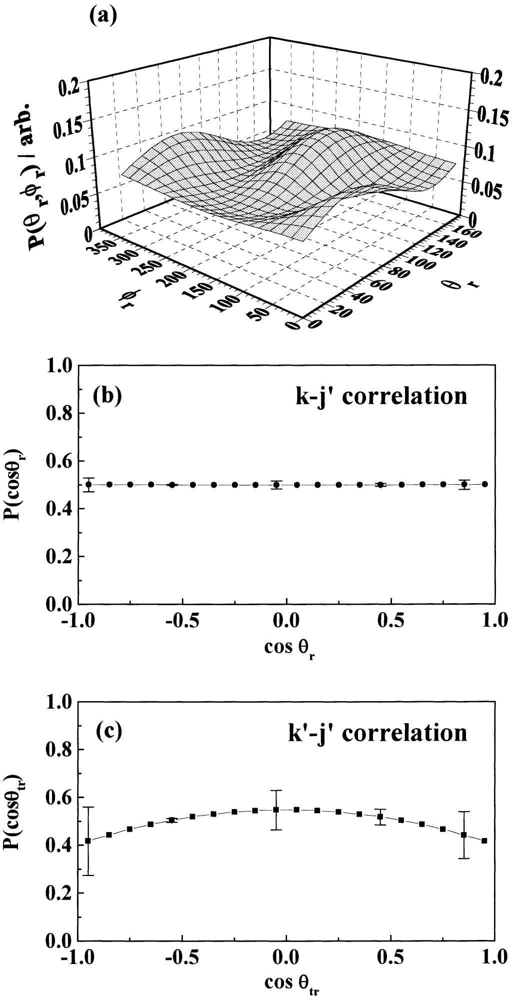

Fig. 21. (a) Angular distribution function $P(\theta_r, \phi_r)$ representing the polarization of the rotational angular momentum vector, $\mathbf{j}'$ for the NO($^2\Pi_{1/2}$, $v' = 0, j' = 34.5$). (b) Angular distribution $P(\theta_r)$ representing the $\mathbf{k}$–$\mathbf{j}'$ correlation. (c) Angular distribution $P(\theta_{tr})$ representing the $\mathbf{k}'$–$\mathbf{j}'$ correlation. The nearly flat angular distribution of $\mathbf{j}'$ with respect to the collision plane shown in (a) arises from the isotropic angular distribution of $\mathbf{j}'$ with respect to both $\mathbf{k}$ and $\mathbf{k}'$ shown in (b) and (c), respectively.

ergy deposited in one bond flows into the other bond in a way depending on the coupling between the two bonds.[197] If the equivalent bonds consist of a heavy central atom and a light terminal atom (hydrogen) such as H_2O and H_2S, the molecular vibration has a local mode character, where the two equivalent vibrations are localized because of relatively weak inter-bond coupling and the strong anhamonicity.[197] On the other hand, the molecules with heavy terminal atoms such as SO_2 have the large momentum coupling and exhibit a normal mode character. Since the ONNO system has the normal mode character due to its mass combination, the efficient energy redistribution in this system can be reasonably expected to occur. The salient features of the O(^{1}D) + N_2O reaction as compared with other reactions mentioned above are the absence of light hydrogen atoms. As analyzed by Akagi et al., the presence of light atoms considerably reduces the momentum coupling among the vibrational modes and significantly retards the energy redistribution.[198] In contrast, the collision complex composed of only heavy atoms possesses low-frequency vibrations to enhance the density of states and large momentum couplings to facilitate the energy randomization. Therefore, in the O(^{1}D) + N_2O reaction, the initial energy deposited between the approaching O(^{1}D) atom and the terminal N atom of the reactant N_2O can flow efficiently into the other vibrational modes. Although we have discussed the energy randomization in terms of the normal mode picture and the inter-mode coupling, our suggestion does not mean that the highly excited vibrational states of ONNO system behave with the regular normal mode character. What we intend to emphasize here is the feasibility of the energy flow in terms of the strength of the vibrational coupling. In the highly excited region near or above the bond-breaking threshold, the normal mode picture does not hold and the level structure becomes irregular. However, it is very plausible that the vibrational motions involving hydrogen atom in X–O–H moiety will tend to be isolated from other modes, compared with the heavy-atom system.

A recent high-level ab initio calculation has shown that a sharp and deep potential well exists near collinear ONNO geometries and that the height of the exit barrier becomes smaller as the O(^{1}D)–N–N angle bends from linear.[199,200] Since the significance of the out-of-plane motion is suggested by the present Doppler study, it is not obvious whether the near statistical behavior is induced by the potential well found in the collinear region obtained by the calculation fixing NNO in the linear shape.[199] A very recently demonstrated ab initio MEP calculated by González et al. presents participation of *trans* and *cis* ONNO pathways.[191] This result is consistent with our observation of isotropic rotational angular momentum polarization of NO products. The future development of the multi-dimensional surface and dynamics calculations will uncover the ambiguities in this reaction.

D. O(^{3}P) + Hydrocarbons. The reactions of the electronically ground-state oxygen atom, O(^{3}P), with hydrocarbons have been attracting great interest in combustion and atmospheric chemistry. Among these, the reactions with alkanes (RH)

$$\mathrm{O}(^3\mathrm{P}) + \mathrm{RH} \rightarrow \mathrm{OH}(^2\Pi) + \mathrm{R}, \tag{21}$$

have been intensively investigated by measuring the rate constants[58,201–203] and product internal state distributions[148,204,205] as well as by QCT calculations.[206,207] It is well recognized that these reactions have activation barriers and no stable intermediates. From such features of PESs, the O(^{3}P) + RH reaction is expected to proceed via a direct pathway.

The OH products are rotationally very cold[148,204] in contrast to the O(^{1}D) reaction with hydrocarbons.[152,154] Andresen et al. showed very good agreement between the observed OH rovibrational distributions[148] and those obtained by QCT calculations on LEPS surfaces constructed for a simple C–H–O triatomic model.[206] The LEPS surfaces giving such agreement favored tight collinear C–H–O configurations. The QCT calculation on this surface naturally predicted the backward scattering of OH products with respect to the incident O(^{3}P) atom. This simple rebound mechanism has long been accepted to account for the cold OH rotational distribution. The calculations, however, approximated the reaction as a triatomic system and neglected the structural features of the reactant hydrocarbons as well as their internal degrees of freedom. Such calculations cannot describe the details of reaction dynamics properly although the simple triatomic picture is still adopted in a recent theoretical work.[207]

The type of C–H bonds in the RH is one of the important factors governing the $O(^3P) + RH$ reaction dynamics, since the exothermicity and activation barrier of these reactions depend on the strength of the C–H bond. The tertiary hydrogen reactions are most exothermic and the primary ones are least exothermic. The activation barriers were estimated to be about 24, 18, and 14 kJ/mol for the abstraction of the primary, secondary, and tertiary hydrogen atoms, respectively.[201,202] The details of the dynamics are therefore dependent on the C–H bond involved.

In the present study, we have measured the DCSs of the OH products in the reactions of $O(^3P)$ with saturated hydrocarbons to directly examine the validity of the rebound mechanism, which has been generally believed.[120] The reaction dynamics of the abstraction of a secondary hydrogen atom has been examined for the reaction of $c\text{-}C_6H_{12}$, whose hydrogen atoms are all secondary ones,

$$O(^3P) + c\text{-}C_6H_{12} \rightarrow OH(^2\Pi) + c\text{-}C_6H_{11} \qquad \Delta H^\circ(0) = -35\ \text{kJ/mol}. \quad (22)$$

The DCSs for this reaction were measured at two different conditions of collision energy distribution to investigate the collision energy dependence. To compare the dynamics of the tertiary hydrogen reaction with that of the secondary hydrogen reaction, we have examined the reaction of $O(^3P)$ with $i\text{-}C_4H_{10}$

$$O(^3P) + i\text{-}C_4H_{10} \rightarrow OH(^2\Pi) + t\text{-}C_4H_9 \qquad \Delta H^\circ(0) = -42\ \text{kJ/mol} \quad (23a)$$

$$\rightarrow OH(^2\Pi) + i\text{-}C_4H_9 \qquad \Delta H^\circ(0) = -19\ \text{kJ/mol}. \quad (23b)$$

The contribution of the primary hydrogen reaction given in Eq. 23b is negligibly small especially in $OH(v' = 1)$ formation since this channel possesses a high activation barrier and yields very cold OH vibrational distribution.[148] Thus, the detection of $OH(v' = 1)$ in the $i\text{-}C_4H_{10}$ reaction extracts the features only for the tertiary hydrogen-atom reaction given in Eq. 23a. In addition, by using the common $O(^3P)$ source, the $i\text{-}C_4H_{10}$ reaction can be compared with the $c\text{-}C_6H_{12}$ reaction at almost the same collision energy since the kinematic conditions of these two reactions are very similar.

We utilized the photolysis of NO_2 at 351 or 308 nm to produce $O(^3P)$ in different translational energies. Figure 22 shows the collision energy distributions employed in our experiment for the reactions of $O(^3P)$ with $c\text{-}C_6H_{12}$ and $i\text{-}C_4H_{10}$. These collision energy distributions are calculated by integrating over all the possible orientation and magnitude of $\mathbf{v_O}$ and $\mathbf{v_{RH}}$ of the collisional encounter, including the effect of thermal motion of precursor NO_2. The details are the same as described in Sec III for generating basis functions. For the $c\text{-}C_6H_{12}$ reaction, the photodissociation of NO_2 at 351 and 308 nm provides different collision energy distributions which have a mean collision energy of $\langle E_{\text{coll}} \rangle = 12$ kJ/mol with a spread of $\Delta E_{\text{coll}} = 17$ kJ/mol in FWHM, and $\langle E_{\text{coll}} \rangle = 33$ kJ/mol with $\Delta E_{\text{coll}} = 35$ kJ/mol, respectively. For the $i\text{-}C_4H_{10}$ reaction, the photodissociation of NO_2 at 308 nm provides a collision energy distribution with $\langle E_{\text{coll}} \rangle = 31$ kJ/mol with $\Delta E_{\text{coll}} = 35$ kJ/mol. Although the whole analysis is performed with the convoluted collision energy distributions, we express the collision energy of each reaction only by $\langle E_{\text{coll}} \rangle$ for simplicity hereafter.

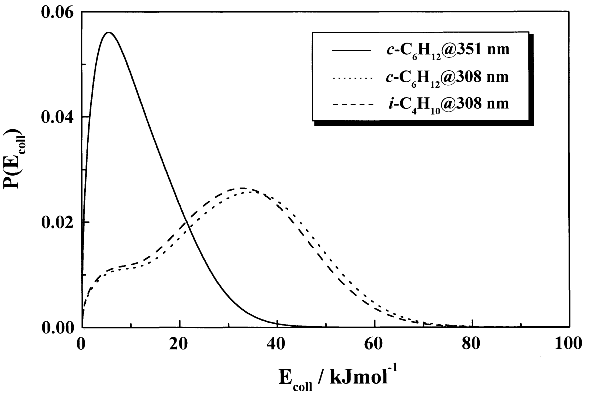

Fig. 22. Collision energy (E_{coll}) distributions in the reactions of $O(^3P)$ with $c\text{-}C_6H_{12}$ and $i\text{-}C_4H_{10}$ initiated by the photodissociation of NO_2 at $\lambda = 351$ and 308 nm. The distributions are calculated by integrating the magnitude and orientation of $\mathbf{v_O}$ and $\mathbf{v_{RH}}$ as generating the basis functions for Doppler analysis. In these calculations, thermal motions of precursor NO_2 and reagent RH are taken into account. The Solid line, $c\text{-}C_6H_{12}$, $\lambda = 351$ nm; the dotted line, $c\text{-}C_6H_{12}$, $\lambda = 308$ nm; and the dashed line, $i\text{-}C_4H_{10}$, $\lambda = 308$ nm.

The observed composite Doppler profiles, $D_0^0(0,\,0;\,v)$ and $D_0^2(2,\,0;\,v)$, for the $OH(^2\Pi_{3/2},\, v' = 1,\, j' = 3.5,\, A')$ formed in the $c\text{-}C_6H_{12}$ and $i\text{-}C_4H_{10}$ reactions are shown in Figs. 23 and 24, respectively. The f_T-averaged DCSs obtained for the $c\text{-}C_6H_{12}$ reaction at $\langle E_{\text{coll}} \rangle = 12$ kJ/mol and 33 kJ/mol are shown in Fig. 25. The DCS measured for low $\langle E_{\text{coll}} \rangle$ shows predominant intensities in the backward hemisphere with respect to the incident $O(^3P)$ atom. The backward scattering suggests the dominance of the rebound mechanism proposed by the previous studies.[148,204–206] By contrast, at high $\langle E_{\text{coll}} \rangle$, the amount of the OH products scattered in the forward hemisphere is close to that in the backward hemisphere. These results show that the increase in the collision energy of the $c\text{-}C_6H_{12}$ reaction increases the amount of the forward component. A similar trend is observed in the recent QCT calculation on an ab initio triatomic C–H–O surface which models $O(^3P) + CH_4$ reaction.[207] Furthermore, a simple line-of-centers model suggests that for the reaction with an activation barrier, the increase in the collision energy allows the collisions with large impact parameters to contribute to the reactive scattering.[208] It should be noted that the f_T distributions of the forward and backward components for the OH products of the $c\text{-}C_6H_{12}$ reaction at high $\langle E_{\text{coll}} \rangle$ are different from each other. This is the significant contrast to the $O(^1D)$ reaction with hydrocarbons and H_2O, where we interpret the forward-backward symmetric an-

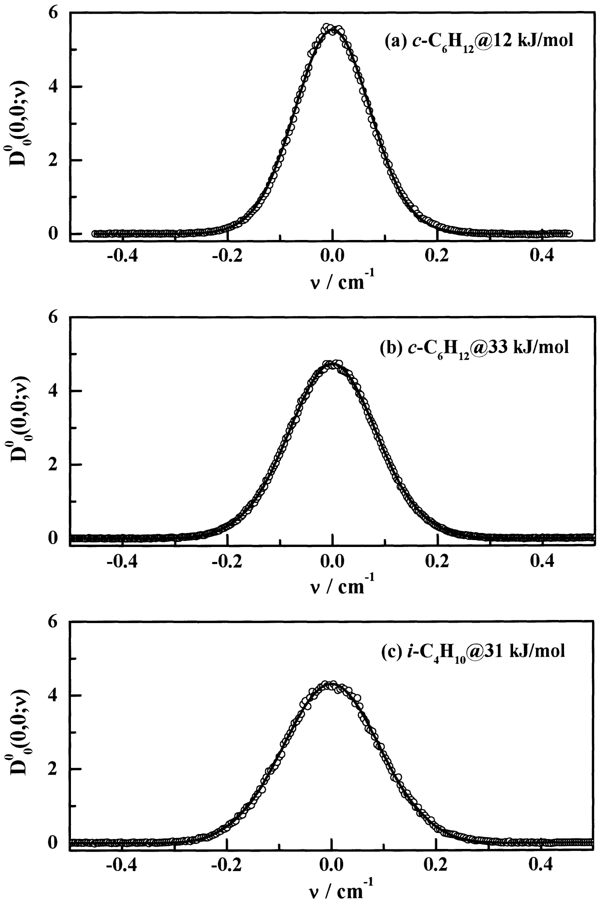

Fig. 23. Observed composite Doppler profiles $D_0^0(0,\,0;\,\nu)$ for the product OH($^2\Pi_{3/2}$, $v' = 1, j' = 3.5$) generated from the reactions of O(^{3}P) with c-C_6H_{12} and i-C_4H_{10}. Smooth solid lines are the best fits in the Doppler analysis.

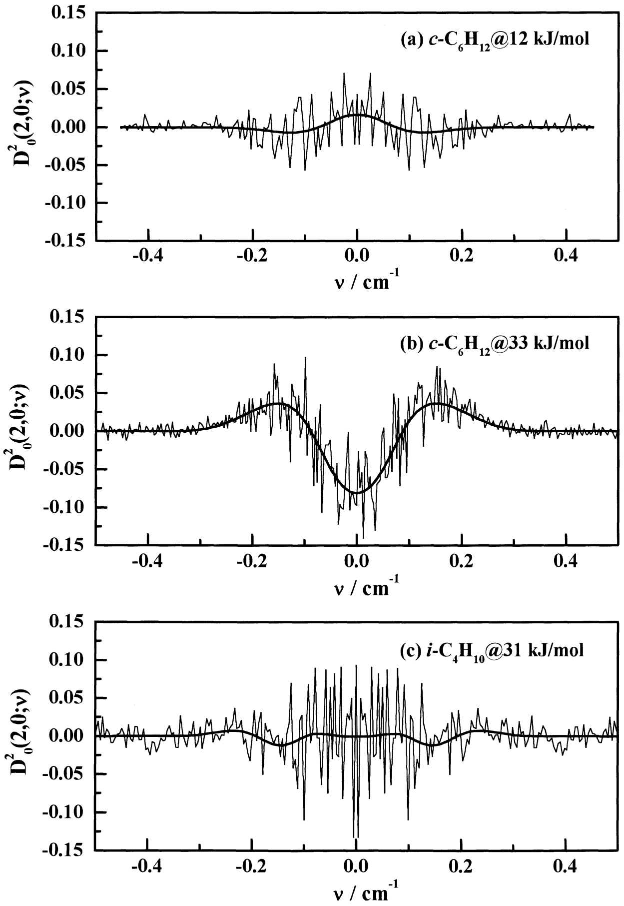

Fig. 24. Observed composite Doppler profiles $D_0^2(2,\,0;\,\nu)$ for the product OH($^2\Pi_{3/2}$, $v' = 1, j' = 3.5$) generated from the reactions of O(^{3}P) with c-C_6H_{12} and i-C_4H_{10}. Smooth solid lines are the best fits in the Doppler analysis.

gular distribution in terms of an insertion mechanism. Based on the QCT calculations by Luntz et al.,[206] the quite cold rotational distributions of the OH products for the reactions of O(^{3}P) with saturated hydrocarbons have been attributed to the dominance of the rebound mechanism.[148,204–206] However, the collision energy dependence of the DCS obtained here demonstrates that the rotationally cold OH products arise not only from the "rebound" pathway but also from the "stripping" pathway. The result shows that the relative contribution of these two pathways to the reactive scattering changes with the collision energy although the cold rotational distribution remains the same. Therefore, the reaction dynamics cannot be characterized only from the rotational distributions of the OH products.

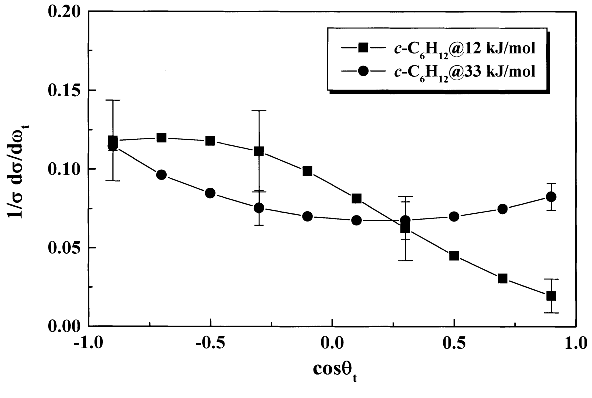

Fig. 25. The DCSs of the product OH($^2\Pi_{3/2}$, $v' = 1, j' = 3.5$) averaged over the whole f_T region in the O(^{3}P) + c-C_6H_{12} reaction at $\langle E_{coll}\rangle = 12$ kJ/mol (■) and 33 kJ/mol (●). Error bars correspond to $\pm 1\sigma$.

The rate constant measurements for O(^{3}P) reactions with i-C_4H_{10} and c-C_6H_{12}[201–203] established that the activation barrier of the i-C_4H_{10} reaction is lower than that of the c-C_6H_{12} reaction, suggesting the higher reactivity of the tertiary hydrogen atom than that of the secondary one. In general, the lower the activation barrier, the higher is the contribution of large impact parameters, at high collision energies. Thus, the forward component arising from large impact parameters is expected to be larger for the i-C_4H_{10} reaction than for the c-C_6H_{12} reaction. Figure 26 compares the DCS of the OH($^2\Pi_{3/2}$, $v' = 1, j' = 3.5$) product in the i-C_4H_{10} reaction with that in the c-C_6H_{12} reaction at almost the same $\langle E_{coll}\rangle \approx 30$ kJ/mol. The DCS for the i-C_4H_{10} reaction shows a broad distribution with a slight preference for sideways scattering. The forward scattering in this reaction is smaller than or similar to that in the c-C_6H_{12} reaction. This trend mainly originates from the difference in the anisot-

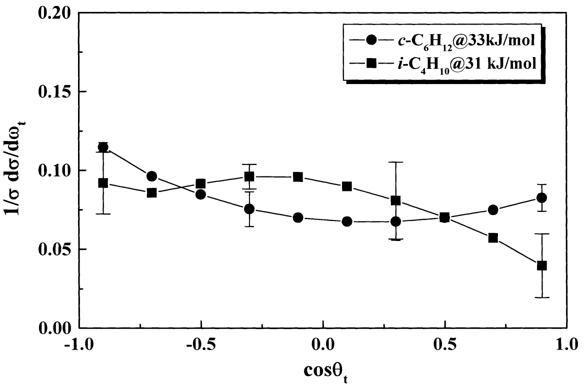

Fig. 26. The DCSs of the product OH ($^2\Pi_{3/2}$, $v' = 1, j' = 3.5$) averaged over the whole f_T region in the reactions of O(^{3}P) with i-C_4H_{10} (■) and c-C_6H_{12} (●) at $\langle E_{coll} \rangle \approx 30$ kJ/mol. Error bars represent $\pm 1\sigma$.

ropy shown in Figs. 24(b) and (c). The absence of the increase in the forward scattering in going from c-C_6H_{12} to i-C_4H_{10} shows that the contribution of large impact parameters is significantly limited in the i-C_4H_{10} reaction in spite of its low activation barrier. This trend, opposing to the expectation from the height of activation barrier, can be explained by the structural feature of the hydrocarbon, especially the environment of the reaction site. The i-C_4H_{10} contains the three bulky methyl groups around the tertiary C–H bond and therefore the steric hindrance around the reaction site in i-C_4H_{10} molecule is larger than around that in c-C_6H_{12}. The large steric hindrance for the i-C_4H_{10} reaction diminishes the advantage of the i-C_4H_{10} reaction to the c-C_6H_{12} reaction as the collision energy increases.

Steric hindrance corresponds to the pre-exponential factor of a rate constant, which expresses a steric factor. Thus the observed trend of the steric hindrance can be considered as the difference in the temperature dependence of the pre-exponential factors. It is found a qualitative agreement between the results obtained in this study and the temperature dependence of the pre-exponential factor of the hydrogen abstraction reaction by O(^{3}P) with secondary and tertiary hydrogen atom.[203] This agreement also implies that the large steric hindrance of i-C_4H_{10} molecule inhibits enlargement of the effective cone-of-acceptance in spite of the increase in the collision energy.

As described in the beginning of this subsection, the triatomic picture has long been accepted for the O(^{3}P) + alkane reactions due to the success of the QCT calculation with this approximation.[206] However, the calculation was only focused on the rovibrational distributions of the product OH. The validity of this approximation should also be evaluated by observing the internal energy (E_{int}) of the co-product alkyl radical. The E_{int} distributions of the cyclohexyl radical produced from the c-C_6H_{12} reactions at $\langle E_{coll} \rangle = 12$ and 33 kJ/mol are derived from the f_T distributions of OH($^2\Pi_{3/2}$, $v' = 1, j' = 3.5$) by integrating their $(1 - f_T)$ distributions over the collision energy distributions. The mean value of E_{int} of the cyclohexyl radical, $\langle E_{int} \rangle$, amounts to more than 60% of that of the available energy for OH($^2\Pi_{3/2}$, $v' = 1, j' = 3.5$) channel. Furthermore, $\langle E_{int} \rangle$ is almost proportional to the increase in $\langle E_{avl} \rangle$. The significant excitation of cyclohexyl radical and the proportionality between $\langle E_{int} \rangle$ and $\langle E_{avl} \rangle$ indicate that the alkyl radical does not behave as a spectator as assumed in the triatomic approximation. This means that the internal degrees of freedom of the hydrocarbon need to be taken into account. The structural change caused by the transformation of alkanes to alkyl radicals should be one of the important factors to determine the extent of the internal excitation of the alkyl radical products. Therefore, these abstraction reactions are not always dominated by the simple rebound mechanism. The large fraction of $\langle E_{int} \rangle$ is also observed in the very recent crossed molecular beam experiment.[209]

V. Concluding Remarks

We have reviewed our recent studies on gas-phase oxygen-atom reaction dynamics. Experimentally, we have measured the vectorial properties, such as product-state resolved scattering angle distribution and rotational angular momentum polarization by utilizing Doppler-resolved polarization spectroscopy. The reaction mechanisms are discussed on the basis of the direct information of such vector properties combined with the scalar information like product-state distributions. For the O(^{1}D) reactions with hydrocarbon and water both forming OH products, there have been some conflicts in the arguments about the reaction mechanisms although the product-state distribution and the presence of the stable intermediate have been well characterized. Our Doppler studies show that the insertion pathway is dominant and the X–O–H (X = C or O) bending motion dominates the torque to rotate OH products. In contrast, the NO products of the O(^{1}D) + N_2O reaction have isotropic rotational angular momentum distribution, indicating the participation of in-plane and out-of-plane motions. The different trends of rotational angular momentum polarization in these reactions are consistent with the opposite trends of the energy partitioning in these reactions, especially, the difference in the degree of energy randomization. The reactions of O(^{3}P) with hydrocarbons are turned out that the simple triatomic picture is not adequate from the DCS at high collision energies and substantial energy flow into alkyl radicals. These findings are never obtained from the product-state measurement alone.

Although the success of our approach is evident, the detailed dynamics of chemical reactions on PESs is not completely uncovered yet. A weakness in our approach is the considerable averaging of collision energy. The oxygen atoms produced via the photodissociation of polyatomic molecules have a spread of translational energy according to the internal energy distribution of the sister fragment and this spread is transferred to that of collision energy in bimolecular encounters under the bulb condition. Due to the spread of the collision energy, we cannot precisely specify the internal energy of the sister products from the translational energy of the observed products. Thus, we have not discussed about the slight difference in the vector correlations among the f_T components. Ideally, the measurement of vector properties has to be performed with the complete state selection of both the observed and sister products under the well-defined collision energies. The correlation measured under such conditions will uncover the reaction dynamics more clearly than the present studies. Preparing sharp collision energies is also important to eliminate the possible mixing of different reaction mechanisms whose contributions depend on the collision energy. In our system, the collision energies of the O(^{1}D) reactions are almost 50 kJ/mol and thus the contributions of the excited states are highly plausible. As discussed in Sec. IV, the observed product OH rovibrational levels of O(^{1}D) reactions with hydrocarbon and water can be considered to reflect the dynamics on the ground state PES. For O(^{1}D) + N_2O reaction, Akagi et al. showed that the ab initio surfaces other than the lowest one have repulsive characters[199] and thus the contribution is not expected to be significant. However, by utilizing monoenergetic H atom production from the photodissociation of HI, Brouard et al. have analyzed the θ_t-resolved $P(\theta_r, \phi_r)$ for H + N_2O (Ref. 94) and H + CO_2 (Ref. 95) reactions with the Doppler LIF method. Thus, to perform the experiments with sharp collision energies is strongly desired.

The requirements of the ideal experiment will be mostly fulfilled if the state-of-the-art experimental techniques reviewed in the beginning of this account are performed by detecting molecular products with polarization analysis. Crossed molecular beam experiment is a promising approach for this purpose although a considerable decrease in signal is the inevitable difficulty. However, this type of recent experiments for inelastic collisions of NO($^2\Pi_\Omega$, v, j) + X → NO($^2\Pi_{\Omega'}$, v', j') + X (X = He, Ar, D_2)[210–213] and HCl + Ar (Ref. 214) exhibit its potential power to elucidate the detailed dynamics of chemical reactions. In fact, Cline and coworkers have measured the polarization of the rotational angular momentum of the inelastically scattered NO molecules.[211,212] In particular, by utilizing circularly polarized probe laser, they have clearly observed the sense of rotation, which satisfactorily agrees to quantum mechanical scattering caluculation.[211] As has been described here, the crossed molecular beam method is essential to elucidate reaction dynamics but this method has limitation to produce high collision energy. Thus, to discuss the effect of large collision energies, the Doppler experiments under the bulb condition will complement the crossed molecular beam experiments.

Does the progress in the experimental measurement alone answer the question of how chemical reactions proceed on PESs? The answer is "No" since experimental observables are physical quantities measured for the separated products after the reaction. Although some sorts of time-resolved measurement can extract the real time dynamics on the PESs,[215] the time-resolved signals represent only a partial aspect of the dynamics which can be optically probed. Furthermore, the interpretation of the observed results in terms of a multi-dimensional potential surface is not straightforward. Therefore, to complement the information obtained by the experiments, the collaboration between experiments and theoretical calculations becomes more important than ever.

The reaction of triatomic system inevitably yields one atomic product and this simple condition enables detailed investigation for this type of reaction both by experiments and theories. However, the triatomic system is too simple to understand how the energetic intermediate breaks up while distributing the stored energy to the various degrees of freedom of molecular products. Thus, to fully uncover the dynamics of tetra-atomic system is desired as the first step in this new century. At present, for the tetra-atomic system of six-dimensional (6D) space, it is still tremendously time consuming to construct the reliable PES and to perform scattering calculations for reasonably high total angular momentum. However, the accurate PES of very simple tetra-atomic system containing hydrogen atoms, such as H + H_2O → H_2 + OH, is obtained[216] by fitting to the high-level extensive ab initio data points and the 6D QCT calculation on this surface has been successful in reproducing the observed rotational angular momentum polarization.[217] The essential understanding of chemical reactions, including much heavier systems as studied here, will be attained in the near future, based on high-quality experimental observations and theoretical calculations. In that stage, it is definitely sure that the important thing is the extraction of the necessary information from the vast amount of calculation results for the multi-dimensional dynamics and not only obtaining the agreement between the experiments and calculations.

References

1 R. D. Levine and R. B. Bernstein, "Molecular Reaction Dynamics and Chemical Reactivity," Oxford University Press, Oxford (1987).

2 R. B. Bernstein, "Chemical Dynamics via Molecular Beam and Laser Techniques," Clarendon Press, Oxford (1982).

3 J. I. Steinfeld, J. S. Franscisco, and W. L. Hase, "Chemical Kinetics and Dynamics," Prentice Hall, New Jersy (1989).

4 M. Brouard, "Reaction Dynamics," Oxford University Press, Oxford (1998).

5 H. Eyring, *J. Chem. Phys.*, **3**, 107 (1935).

6 R. P. Wayne, "Chemistry of Atmospheres, An Introduction to the Chemistry of the Atmospheres of Earth, the Planets and their Satellites," Oxford University Press, Oxford (1991).

7 W. C. Gardiner Jr. ed "Combustion Chemistry," Springer-Verlag, New York (1984).

8 R. N. Zare, *Science*, **279**, 1875 (1998).

9 M. G. Evans and M. Polanyi, *Trans. Faraday Soc.*, **35**, 178 (1939).

10 N. F. Ramsey, "Molecular Beams," Oxford University Press, Oxford (1956).

11 G. Scoles ed, "Atomic and Molecular Beam Methods Volume I," Oxford University Press, Oxford (1988).

12 I. W. M. Smith, "Kinetics and Dynamics of Elementary Gas Reactions," Butterworths, London (1980).

13 S. Glasstone, K. J. Laidler, and H. Eyring, "The Theory of Rate Processes," McGraw-hill, New York (1941).

14 D. R. Herschbach, *Adv. Chem. Phys.*, **10**, 319 (1966).

15 J. C. Polanyi, *Acc. Chem. Res.*, **5**, 161 (1972).

16 K. P. Lawley ed, "Molecular Scattering: Physical and Chemical Applications," *Adv. Chem. Phys.*, **30**, Wiley-Interscience, London (1975).

17 J. C. Polanyi, *Science*, **263**, 680 (1987).

18 Y. T. Lee, *Science*, **263**, 793 (1987).

19 W. Demtröder, "Laser Spectroscopy, Basic Concepts and Instrumentation," Springer-Verlag, Berlin (1981).

20 P. Casavecchia, N. Balucani, and G. G. Volpi, in "The Chemical Dynamics and Kinetics of Small Molecules Part I," ed by K. Liu and A. Wagner, World Scientific, Singapore (1995).

21 P. Casavecchia, N. Balucani, and G. G. Volpi, *Annu. Rev. Phys. Chem.*, **50**, 437 (1999).

22 J. J. Lin, D. W. Hwang, S. Harich, Y. T. Lee, and X. Yang, *Rev. Sci. Insrum.*, **69**, 1642 (1998).

23 R. N. Zare and P. J. Dagdigian, *Science*, **185**, 739 (1974).

24 S. R. Leone, *Annu. Rev. Phys. Chem.*, **35**, 109 (1984).

25 S. R. Leone, *Science*, **227**, 889 (1985).

26 W. D. Lawrence, C. B. Moore, and H. Petek, *Science*, **227**, 895 (1985).

27 M. N. R. Ashfold and J. E. Baggott eds, "Molecular Photodissociation Dynamics," The Royal Society of Chemistry, London (1987).

28 T. Baer and W. L. Hase, "Unimolecular Reaction Dynamics, Theory and Experiments," Oxford University Press, Oxford (1996).

29 R. N. Zare and D. R. Herschbach, *Proc. IEEE*, **51**, 173 (1963).

30 D. A. Case, G. M. McClelland, and D. R. Herschbach, *Mol. Phys.*, **35**, 541 (1978).

31 C. H. Greene and R. N. Zare, *J. Chem. Phys.*, **78**, 6741 (1983).

32 R. N. Dixon, *J. Chem. Phys.*, **85**, 1866 (1986).

33 G. E. Hall, N. Sivakumar, D. Chawla, P. L. Houston, and I. Burak, *J. Chem. Phys.*, **88**, 3682 (1988).

34 R. J. Gordon and G. E. Hall, *Adv. Chem. Phys.*, **96**, 1 (1996).

35 "Dynamical Stereochemistry Issue," *J. Phys. Chem.*, **91**, 5365 (1987).

36 "Orientation and Polarisation Effects in Reactive Collisions," *J. Chem. Soc., Faraday Trans. 2*, **85**, 925 (1989).

37 "Orientation and Polarisation Effects in Chemical Reaction Dynamics," *J. Chem. Soc., Faraday Trans.*, **89**, 1401 (1993).

38 "Stereodynamics and Active Control in Chemical Reactions," *J. Phys. Chem.*, **99**, 13569 (1995).

39 A. J. Orr-Ewing, *J. Chem. Soc., Faraday Trans.*, **92**, 881, (1996).

40 L. Schnieder, K. Seekamp-Rahn, J. Borkowski, E. Wrede, K. H. Welge, F. J. Aoiz, L. Bañares, M. J. D'Mello, V. J. Herrero, V. S. Rábanos, and R. E. Wyatt, *Science*, **269**, 207 (1995).

41 L. Schnieder, W. Meier, K. H. Welge, M. N. R. Ashofold, and C. M. Western, *J. Chem. Phys.*, **92**, 7027 (1990).

42 E. Wrede, L. Schnieder, K. H. Welge, F. J. Aoiz, L. Bañares, and V. J. Herrero, *Chem. Phys. Lett.*, **265**, 129 (1997).

43 E. Wrede, L. Schnieder, K. H. Welge, F. J. Aoiz, L. Bañares, V. J. Herrero, B. Martínez-Haya, and V. S. Rábanos, *J. Chem. Phys.*, **106**, 7862 (1997).

44 E. Wrede and L. Schnieder, *J. Chem. Phys.*, **107**, 786 (1997).

45 L. Schnieder, K. Seekamp-Rahn, E. Wrede, and K. H. Welge, *J. Chem. Phys.*, **107**, 6175 (1997).

46 X. Liu, J. J. Lin, S. A. Harich, and X. Yang, *J. Chem. Phys.*, **113**, 1325 (2000).

47 X. Liu, J. J. Lin, S. A. Harich, G. C. Schatz, and X. Yang, *Science*, **289**, 1536 (2000).

48 D.-C. Che and K. Liu, *J. Chem. Phys.*, **103**, 5164 (1995).

49 Y.-T. Hsu and K. Liu, *J. Chem. Phys.*, **107**, 1664 (1997).

50 Y.-T. Hsu, J.-H. Wang, and K. Liu, *J. Chem. Phys.*, **107**, 2351 (1997).

51 Y.-T. Hsu, K. Liu, L. A. Pederson, and G. C. Schatz, *J. Chem. Phys.*, **111**, 7921 (1999).

52 Y.-T. Hsu, K. Liu, L. A. Pederson, and G. C. Schatz, *J. Chem. Phys.*, **111**, 7931 (1999).

53 P. Hermine, Y.-T. Hsu, and K. Liu, *Phys. Chem. Chem. Phys.*, **2**, 581 (2000).

54 G. C. Schatz, *Science*, **288**, 1599 (2000).

55 R. T. Skodje, D. Skouteris, D. E. Manolopoulos, S.-H. Lee, F. Dong, and K. Liu, *J. Chem. Phys.*, **112**, 4526 (2000).

56 F. J. Aoiz, L. Bañares, and V. J. Herrero, *J. Chem. Soc., Faraday Trans.*, **94**, 2483 (1998).

57 S. A. Kandel, A. J. Alexander, Z. H. Kim, R. N. Zare, F. J. Aoiz, L. Bañares, J. F. Castillo, and V. S. Rábanos, *J. Chem. Phys.*, **112**, 670 (2000).

58 N. Cohen and K. R. Westberg, *J. Phys. Chem. Ref. Data*, **20**, 1211 (1991).

59 D. L. Baulch, C. J. Cobos, R. A. Cox, C. Esser, P. Frank, Th. Just, J. A. Kerr, M. J. Pilling, J. Troe, R. W. Walker, and J. Warnatz, *J. Phys. Chem. Ref. Data*, **21**, 411 (1992).

60 R. Atkinson, D. L. Baulch, R. A. Cox, R. F. Hampson, Jr., J. A. Kerr, and J. Troe, *J. Phys. Chem. Ref. Data*, **21**, 1125 (1992).

61 J. P. Simons, *J. Phys. Chem.*, **91**, 5378 (1987).

62 P. L. Houston, *J. Phys. Chem.*, **91**, 5388 (1987).

63 G. E. Hall and P. L. Houston, *Annu. Rev. Phys. Chem.*, **40**, 375 (1989).

64 R. Schinke, "Photodissociation Dynamics," Chambridge University Press, Cambridge (1993).

65 C. Jonah, *J. Chem. Phys.*, **55**, 1915 (1971).

66 M. Mons and I. Dimicoli, *J. Chem. Phys.*, **90**, 4037 (1989).

67 R. Uberna, R. D. Hinchliffe, and J. I. Cline, *J. Chem. Phys.*, **103**, 7934 (1995).

68 A. J. R. Heck and D. W. Chandler, *Annu. Rev. Phys. Chem.*, **46**, 335 (1995).

69 A. G. Suits and R. E. Continetti eds, "Imaging in Chemical Dynamics," American Chemical Society, Washington (2001).

70 "Semiclassical" means that the rotational angular momentum is regarded as a classical vector. In this sense, the angle between **j** and a certain axis can be specified without ambiguity. In quantum mechanical expression, the expectation value of the angular distribution of **j** is obtained as the ensemble average of m_j distribution for spherical tensor operators.

71 M. P. Docker, *Chem. Phys.*, **135**, 405 (1989).

72 A. J. Orr-Ewing and R. N. Zare, *Annu. Rev. Phys. Chem.*, **45**, 315 (1994).

73 M. Brouard and J. P. Simons, in "The Chemical Dynamics and Kinetics of Small Molecules Part II," ed by K. Liu and A. Wagner, World Scientific, Singapore (1995).

74 A. J. Orr-Ewing and R. N. Zare, in "The Chemical Dynamics and Kinetics of Small Molecules Part II," ed by K. Liu and A. Wagner, World Scientific, Singapore (1995).

75 A. J. Alexander and R. N. Zare, *J. Chem. Educ.*, **75**, 1105 (1998).

76 J. P. Simons, *Faraday Discuss.*, **113**, 1 (1999).

77 N. E. Shafer, A. J. Orr-Ewing, W. R. Simpson, H. Xu, and R. N. Zare, *Chem. Phys. Lett.*, **212**, 155 (1993).

78 N. E. Shafer-Ray, A. J. Orr-Ewing, and R. N. Zare, *J. Phys. Chem.*, **99**, 7591 (1995).

79 K. Kleinermanns and E. Linnebach, *Appl. Phys. B*, **36**, 203 (1985).

80 K. Kleinermanns and E. Linnebach, *J. Chem. Phys.*, **82**, 5012 (1985).

81 H. L. Kim, M. A. Wickramaaratchi, X. Zheng, and G. E. Hall, *J. Chem. Phys.*, **101**, 2033 (1994).

82 F. J. Aoiz, M. Brouard, P. A. Enriquez, and R. Sayos, *J. Chem. Soc., Faraday Trans.*, **89**, 1427 (1993).

83 F. J. Aoiz, M. Brouard, and P.A. Enriquez, *J. Chem. Phys.*, **105**, 4964 (1996).

84 T. P. Rakitzis, S. A. Kandel, and R. N. Zare, *J. Chem. Phys.*, **107**, 9382 (1997).

85 M. Brouard, S. P. Duxon, P. A. Enriquez, R. Sayos, and J. P. Simons, *J. Phys. Chem.*, **95**, 8169 (1991).

86 F. Green, G. Hancock, A. J. Orr-Ewing, M. Brouard, S. P. Duxon, P. A. Enriquez, R. Sayos, and J. P. Simons, *Chem. Phys. Lett.*, **182**, 568 (1991).

87 M. Brouard, S. P. Duxon, P. A. Enriquez, and J. P. Simons, *J. Chem. Phys.*, **97**, 7414 (1992).

88 M. Brouard, S. Duxon, P. A. Enriquez, and J. P. Simons, *J. Chem. Soc., Faraday Trans.*, **89**, 1435 (1993).

89 M. Brouard, S. P. Duxon, and J. P. Simons, *Isr. J. Chem.*, **34**, 67 (1994).

90 M. Brouard, H. M. Lambert, J. Short, and J. P. Simons, *J. Phys. Chem.*, **99**, 13751 (1995).

91 A. J. Alexander, M. Brouard, S. P. Rayner, and J. P. Simons, *Chem. Phys.*, **207**, 215 (1996).

92 M. Brouard, H. M. Lambert, S. P. Rayner, and J. P. Simons, *Mol. Phys.*, **89**, 403 (1996).

93 A. J. Alexander, F. J. Aoiz, L. Bañares, M. Brouard, J. Short, and J. P. Simons, *J. Phys. Chem. A*, **101**, 7544 (1997).

94 M. Brouard, S. D. Gatenby, D. M. Joseph, and C. Vallance, *J. Chem. Phys.*, **113**, 3162 (2000).

95 M. Brouard, I. Burak, D. W. Hughes, K. S. Kalogerakis, J. P. Simons, and V. Stavros, *J. Chem. Phys.*, **113**, 3173 (2000).

96 M. L. Costen, G. Hancock, A. J. Orr-Ewing, and D. Summerfield, *J. Chem. Phys.*, **100**, 2754 (1994).

97 M. L. Costen, G. Hancock, and G. A. D. Ritchie, *J. Phys. Chem. A*, **103**, 10651 (1999).

98 R. Fei, X. S. Zheng, and G. E. Hall, *J. Phys. Chem. A*, **101**, 2541 (1997).

99 A. J. Orr-Ewing, W. R. Simpson, T. P. Rakitzis, S. A. Kandel, and R. N. Zare, *J. Chem. Phys.*, **106**, 5961 (1997).

100 T. P. Rakitzis, S. A. Kandel, T. Lev-On, and R. N. Zare, *J. Chem. Phys.*, **107**, 9392 (1997).

101 H. Tsurumaki, Y. Fujimura, and O. Kajimoto, *Chem. Phys. Lett.*, **301**, 145 (1999).

102 H. Tsurumaki, Y. Fujimura, and O. Kajimoto, *J. Chem. Phys.*, **110**, 7707 (1999).

103 H. Tsurumaki, Y. Fujimura, and O. Kajimoto, *J. Chem. Phys.*, **111**, 592 (1999).

104 H. Akagi, H. Tsurumaki, Y. Fujimura, and O. Kajimoto, *Z. Phys. Chem.*, **215**, 1137 (2001).

105 H. Tsurumaki, Y. Fujimura, and O. Kajimoto, in preparation.

106 R. Ogorzalek Loo, G. E. Hall, H.-P. Haerri, and P. L. Houston, *J. Phys. Chem.*, **92**, 5 (1988).

107 W. R. Simpson, A. J. Orr-Ewing, T. P. Rakitzis, S. A. Kandel, and R. N. Zare, *J. Chem. Phys.*, **103**, 7299 (1995).

108 M. H. Alexander and P. J. Dagdigian, *J. Chem. Phys.*, **80**, 4325 (1984).

109 M. H. Alexander et al., *J. Chem. Phys.*, **89**, 1749 (1988).

110 M. Brouard, H. M. Lambert, C. L. Russell, J. Short, and J. P. Simons, *Faraday Discuss.*, **102**, 179 (1995).

111 A. J. Alexander, F. J. Aoiz, M. Brouard, I. Burak, Y. Fujimura, J. Short, and J. P. Simons, *Chem. Phys. Lett.*, **262**, 589 (1996).

112 A. J. Alexander, D. A. Blunt, M. Brouard, J. P. Simons, F. J. Aoiz, L. Bañares, Y. Fujimura, and M. Tsubouchi, *Faraday Discuss.*, **108**, 375 (1997).

113 D. S. King, D. G. Sauder, and M. P. Casassa, *J. Chem. Phys.*, **97**, 5919 (1992).

114 M. Brouard, D. W. Hughes, K. S. Kalogerakis, and J. P. Simons, *J. Phys. Chem.*, **102**, 9559 (1998).

115 M. Brouard, I. Burak, G. A. J. Markillie, K. McGrath, and C. Vallance, *Chem. Phys. Lett.*, **281**, 97 (1997).

116 M. Brouard, I. Burak, D. M. Joseph, G. A. J. Markillie, D. Minayev, P. O'Keeffe, and C. Vallance, *J. Chem. Phys.*, **114**, 6690 (2001).

117 M. Brouard, I. Burak, S. D. Gatenby, and G. A. J. Markillie, *Chem. Phys. Lett.*, **287**, 682 (1998).

118 M. Brouard, I. Burak, S. D. Gatenby, D. Hart, and D. Minayev, *J. Chem. Phys.*, **110**, 11335 (1999).

119 K. Honma and Y. Tsutsui, *Chem. Phys. Lett.*, **309**, 35 (1999).

120 H. Tsurumaki, Y. Fujimura, and O. Kajimoto, *J. Chem. Phys.*, **112**, 8338 (2000).

121 W. R. Simpson, A. J. Orr-Ewing, and R. N. Zare, *Chem. Phys. Lett.*, **212**, 163 (1993).

122 W. R. Simpson, T. P. Rakitzis, S. A. Kandel, A. J. Orr-Ewing, and R. N. Zare, *J. Chem. Phys.*, **103**, 7313 (1995).

123 W. R. Simpson, T. P. Rakitzis, S. A. Kandel, T. Lev-On, and R. N. Zare, *J. Phys. Chem.*, **100**, 7938 (1996).

124 S. A. Kandel, T. P. Rakitzis, T. Lev-On, and R. N. Zare, *J. Chem. Phys.*, **105**, 7550 (1996).

125 S. A. Kandel, T. P. Rakitzis, T. Lev-On, and R. N. Zare, *Chem. Phys. Lett.*, **265**, 121 (1996).

126 S. A. Kandel, T. P. Rakitzis, T. Lev-On, and R. N. Zare, *J. Phys. Chem. A*, **102**, 2270 (1998).

127 H. Xu, N. E. Shafer-Ray, F. Merkt, D. J. Hughes, M. Springer, R. P. Tuckett, and R. N. Zare, *J. Chem. Phys.*, **103**, 5157 (1995).

128 F. Fernández-Alonso, B. D. Bean, and R. N. Zare, *J. Chem. Phys.*, **111**, 1022 (1999).

129 F. Fernández-Alonso, B. D. Bean, and R. N. Zare, *J. Chem. Phys.*, **111**, 1035 (1999).

130 F. Fernández-Alonso, B. D. Bean, and R. N. Zare, *J. Chem. Phys.*, **111**, 2490 (1999).

131 A. Eppink and D. H. Parker, *Rev. Sci. Instrum.*, **68**, 3477 (1997).

132 K. Chen, K. Lee, J. Chang, C. Sung, T. Chung, T. Liu, and H. Perng, *J. Phys. Chem.*, **100**, 488 (1996).

133 M. L. Costen, S. W. North, and G. E. Hall, *J. Chem. Phys.*, **111**, 6735 (1999).

134 W. J. van der Zande, R. Zhang, R. N. Zare, K. G. McKendrick, and J. J. Valentini, *J. Phys. Chem.*, **95**, 8205 (1991).

135 E. de Beer, M. P. Koopmans, C. A. de Lange, Y. Wang, and W. A. Chupka, *J. Chem. Phys.*, **94**, 7634 (1991).

136 R. Altkorn and R. N. Zare, *Annu. Rev. Phys. Chem.*, **35**, 265 (1984).

137 R. N. Zare, "Angular Momentum, Understanding Spatial Aspects in Chemistry and Physics," Wiley-Interscience, New York (1988).

138 Strictly speaking, $\beta_Q^K(k_1k_2)$ is a renormalize bipolar moment, whose maximum of absolute value is scaled to 1.

139 P. Felder, B.-M. Haas, and J. R. Huber, *Chem. Phys. Lett.*, **186**, 177 (1991).

140 L. L. Springsteen, S. Satyapal, Y. Matsumi, L. M. Dobeck, and P. L. Houston, *J. Phys. Chem.*, **97**, 7239 (1993).

141 T. Suzuki, H. Katayanagi, Y. Mo, and K. Tonokura, *Chem. Phys. Lett.*, **256**, 90 (1996).

142 D. W. Neyer, A. J. R. Heck, and D. W. Chandler, *J. Chem. Phys.*, **110**, 3411 (1999).

143 D. W. Neyer, A. J. R. Heck, D. W. Chandler, J. M. Teule,

and M. H. M. Janssen, *J. Phys. Chem. A*, **103**, 10388 (1999).

144 H. Zacharias, K. Meirer, and K. H. Welge, in "Energy Storage and Redistribution in Molecules," ed by J. Hinze, Plenum, New York (1983).

145 R. P. Baker, M. L. Costen, G. Hancock, G. A. D. Ritchie, and D. Summerfield, *Phys. Chem. Chem. Phys.*, **2**, 661 (2000).

146 M. Ahmed, E. R. Wouters, D. S. Peterka, O. S. Vasyutinskii, and A. G. Suits, *Faraday Discuss.*, **113**, 425 (1999)

147 W. H. Press, B. P. Flannery, S. A. Teukolsky, and W. T. Vetterling, "Numerical Recipes in C 2nd ed.," Cambridge University Press, Cambridge (1992).

148 P. Andresen and A. C. Luntz, *J. Chem. Phys.*, **72**, 5842 (1980).

149 H. Yamazaki and R. J. Cvetanovic, *J. Chem. Phys.*, **41**, 3703 (1964).

150 G. Paraskevopoulos and R. J. Cvetanovic, *J. Chem. Phys.*, **50**, 590 (1969).

151 G. Paraskevopoulos and R. J. Cvetanovic, *J. Chem. Phys.*, **52**, 5821 (1970).

152 A. C. Luntz, *J. Chem. Phys.*, **73**, 1143 (1980).

153 P. M. Aker, J. J. A. O'Brien, and J. J. Sloan, *J. Chem. Phys.*, **84**, 745 (1986).

154 C. R. Park and J. R. Wiesenfeld, *J. Chem. Phys.*, **95**, 8166 (1991).

155 S. Wada and K. Obi, *J. Phys. Chem. A*, **102**, 3481 (1998).

156 M. González, M. P. Puyuelo, J. Hernando, R. Sayós, P. A. Enríquez, J. Guallar, and I. Baños, *J. Phys. Chem. A*, **104**, 521 (2000).

157 M. González, M. P. Puyuelo, J. Hernando, R. Sayós, P. A. Enríquez, and J. Gualler, *J. Phys. Chem. A*, **105**, 9834 (2001).

158 J. J. Lin, J. Shu, Y. T. Lee, and X. Yang, *J. Chem. Phys.*, **113**, 5287 (2000).

159 J. Shu, J. J. Lin, Y. T. Lee, and X. Yang, *J. Chem. Phys.*, **114**, 4 (2001).

160 M. González, J. Hernando, I. Baños, and R. Sayós, *J. Chem. Phys.*, **111**, 8913 (1999).

161 M. González, J. Hernando, M. P. Puyuelo, and R. Sayós, *J. Chem. Phys.*, **113**, 6748 (2000).

162 R. Sayós, J. Hernando, M. P. Puyuelo, P. A. Enríquez, and M. González, *Phys. Chem. Chem. Phys.*, **4**, 288 (2002).

163 H. Arai, S. Kato, and S. Koda, *J. Phys. Chem.*, **98**, 12 (1994).

164 O. Kajimoto, H. Yamasaki, and T. Fueno, *Chem. Phys. Lett*,. **68**, 127 (1979).

165 K. Honma, *J. Chem. Phys.*, **99**, 7677 (1993).

166 T. Fueno, Y. Takahara, and K. Yamaguchi, *Chem. Phys. Lett.*, **167**, 291 (1990).

167 J. E. Butler, L. D. Talley, G. K. Smith, and M. C. Lin, *J. Chem. Phys.*, **74**, 4501 (1981).

168 K.-H. Gericke, F. J. Comes, and R. D. Levine, *J. Chem. Phys.*, **74**, 6106 (1981).

169 F. J. Comes, K.-H. Gericke, and J. Manz, *J. Chem. Phys.*, **75**, 2853 (1981).

170 W. A. Guillory, K.-H. Gericke, and F. J. Comes, *J. Chem. Phys.*, **78**, 5993 (1983).

171 C. B. Cleveland and J. R. Wiesenfeld, *J. Chem. Phys.*, **96**, 248 (1992).

172 D. G. Sauder, J. C. Stephenson, D. S. King, and M. P. Casassa, *J. Chem. Phys.*, **97**, 952 (1992).

173 D. S. King, D. G. Sauder, and M. P. Casassa, *J. Chem. Phys.*, **100**, 4200 (1994).

174 N. Tanaka, M. Takayanagi, and I. Hanazaki, *Chem. Phys. Lett.*, **254**, 40 (1996).

175 N. Tanaka, U. Nagashima, M. Takayanagi, H. L. Kim, and I. Hanazaki, *J. Phys. Chem. A*, **101**, 507 (1997).

176 K. Imura, M. Veneziani, T. Kasai, and R. Naaman, *J. Chem. Phys.*, **111**, 4025 (1999).

177 R. Sayós, C. Oliva, and M. González, *J. Chem. Phys.*, **113**, 6736 (2000).

178 R. Sayós, C. Oliva, and M. González, *J. Chem. Phys.*, **115**, 8828 (2001).

179 C. R. Boxall, J. P. Simons, and P. W. Tasker, *Faraday Discuss. Chem. Soc.*, **53**, 182 (1972).

180 G. A. Chamberlain and J. P. Simons, *J. Chem. Soc., Faraday Trans. 2*, **71**, 402 (1975).

181 N. Goldstein, G. D. Greenblatt, and J. R. Wiesenfeld, *Chem. Phys. Lett.*, **96**, 410 (1983).

182 K. Honma, Y. Fujimura, O. Kajimoto, and G. Inoue, *J. Chem. Phys.*, **88**, 4739 (1988).

183 H. Akagi, Y. Fujimura, and O. Kajimoto, *J. Chem. Soc., Faraday Trans.*, **94**, 1575 (1998).

184 H. Akagi, Y. Fujimura, and O. Kajimoto, *J. Chem. Phys.*, **111**, 115 (1999).

185 P. J. Pisano, M. S. Westley, and P. L. Houston, *Chem. Phys. Lett.*, **318**, 385 (2000).

186 Recent measurement in our laboratory shows that the rotational distribution of NO($v' = 0$) is described with $T_{\rm rot} \approx 15000$ K up to $j' \approx 80$ ($E_{\rm rot} \approx 12000$ cm^{-1}) and the distribution seems to sharply decrease around $j' \approx 80$–90.

187 H. Ishikawa, Y. Fujimura, K. Honma, and O. Kajimoto, unpublished.

188 S. G. Kukolich, *J. Am. Chem. Soc.*, **104**, 4715 (1982).

189 A. R. W. McKeller, J. K. G. Watson, and B. J. Howard, *Mol. Phys.*, **86**, 273 (1995).

190 I. Last, A. Aguilar, R. Sayós, M. González, and M. Gilibert, *J. Phys. Chem. A*, **101**, 1206 (1997).

191 M. González, R. Valero, J. M. Anglada, Oliva, and R. Sayós, *J. Chem. Phys.*, **115**, 7015 (2001).

192 J. R. Hetzler, M. P. Casassa, and D. S. King, *J. Phys. Chem.*, **95**, 8086 (1991).

193 M. Ben-Nun, M. Brouard, J. P. Simons, and R. D. Levine, *Chem. Phys. Lett.*, **210**, 423 (1993).

194 M. D. Brookes, A. R. W. McKellar, and T. Amano, *J. Mol. Spectrosc.*, **185**, 153 (1997).

195 G. C. Schatz, M. S. Fitzcharles, and L. B. Harding, *Faraday Discuss. Chem. Soc.*, **84**, 359 (1987).

196 G. Radhakrishnan, S. Buelow, and C. Wittig, *J. Chem. Phys.*, **84**, 727 (1986).

197 M. S. Child, *Acc. Chem. Res.*, **18**, 45 (1985).

198 H. Akagi, Y. Fujimura, and O. Kajimoto, *J. Chem. Phys.*, **110**, 7264 (1999).

199 H. Akagi, A. Yokoyama, Y. Fujimura, and T. Takayanagi, *Chem. Phys. Lett.*, **324**, 423 (2000).

200 T. Takayanagi and A. Wada, *Chem. Phys.*, **269**, 37 (2001).

201 J. T. Herron and R. E. Huie, *J. Phys. Chem.*, **73**, 3327 (1969).

202 P. Kim and R. B. Timmons, *Int. J. Chem. Kinet.*, **7**, 143 (1975).

203 A. Miyoshi, K. Tsuchiya, N. Yamauchi, and H. Matsui, *J. Phys. Chem.*, **98**, 11452 (1994).

204 G. M. Sweeney, A. Watson, and K. G. McKendrick, *J. Chem. Phys.*, **106**, 9172 (1997).

205 G. M. Sweeney and K. G. McKendrick, *J. Chem. Phys.*, **106**, 9182 (1997).
206 A. C. Luntz and P. Andresen, *J. Chem. Phys.*, **72**, 5851 (1980).
207 M. González, J. Hernando, J. Millán, and R. Sayós, *J. Chem. Phys.*, **110**, 7326 (1999).
208 R. D. Levine and R. B. Bernstein, *Chem. Phys. Lett.*, **105**, 467 (1984).
209 X. Liu, R. L. Gross, and A. G. Suits, *J. Chem. Phys.*, **116**, 5341 (2002).
210 M. S. Westley, K. T. Lorenz, D. W. Chandler, and P. L. Houston, *J. Chem. Phys.*, **114**, 2669 (2001).
211 K. T. Lorenz, D. W. Chandler, J. W. Barr, W. Chen, G. L. Barnes, and J. I. Cline, *Science*, **293**, 2063 (2001).
212 J. I. Cline, K. T. Lorenz, E. A. Wade, J. W. Barr, and D. W. Chandler, *J. Chem. Phys.*, **115**, 6277 (2001).
213 H. Kohguchi, T. Suzuki and M. H. Alexander, *Science.*, **294**, 832 (2001).
214 K. T. Lorenz, M. S. Westley, and D. W. Chandler, *Phys. Chem. Chem. Phys.*, **2**, 481 (2000).
215 A. H. Zewail, “Femtochemistry, Ultrafast Dynamics of the Chemical Bond,” World Scientific, Singapore (1994).
216 A. D. Isaacson, *J. Chem. Phys.*, **107**, 3832 (1997).
217 K. S. Bradley and G. C. Schatz, *J. Chem. Phys.*, **108**, 7994 (1998).

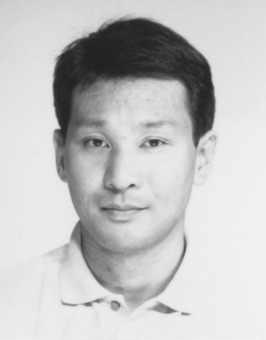

Yo Fujimura was born in Tokyo, Japan, in 1962. He received his degree of D.Sc. at the University of Tokyo under the direction of Professor Okitsugu Kajimoto in 1991. He was a Research Fellow of the Japan Society for the Promotion of Science from 1990 to 1991. He has been a Research Associate at the Department of Chemistry, Kyoto University, since 1991. His research interests are chemical reaction dynamics of gas-phase elementary reactions, especially stereodynamics and the origin of statistical character.

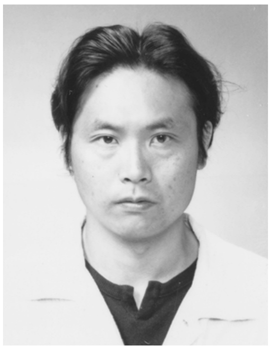

Hiroshi Tsurumaki was born in Niigata, Japan, in 1967. He received his degree of D.Sc. at Kyoto University under the direction of Professor Okitsugu Kajimoto in 1999. He has been a Research Associate at the Department of Electrical Engineering, Kyushu Institute of Technology, since 1999.

Okitsugu Kajimoto was born in Osaka, Japan, in 1942. He received his B.S. and M.S. degrees from Kyoto University and then completed his Ph.D. at Osaka University under the direction of Takayuki Fueno. At Osaka University, he studied elementary gas-phase reactions and energy transfer at high temperatures with shock tube technique. He then worked with Robert Cvetanović at National Research Council of Canada on the reactions of electronically excited species. In 1981, he moved to the University of Tokyo as Associate Professor and started the study of intracluster reactions using supersonic jet technique. He then joined the Graduate School of Science at Kyoto University and has been a Professor of Chemistry since 1990.